

AD-A129 277

127 MICROMETERS RECEIVER DEVELOPMENT(U) ROCKWELL
INTERNATIONAL THOUSAND OAKS CA MICROELECTRONICS RESE..
H D LAW ET AL. MAR 83 MRDC41031.5FR RADC-TR-83-66

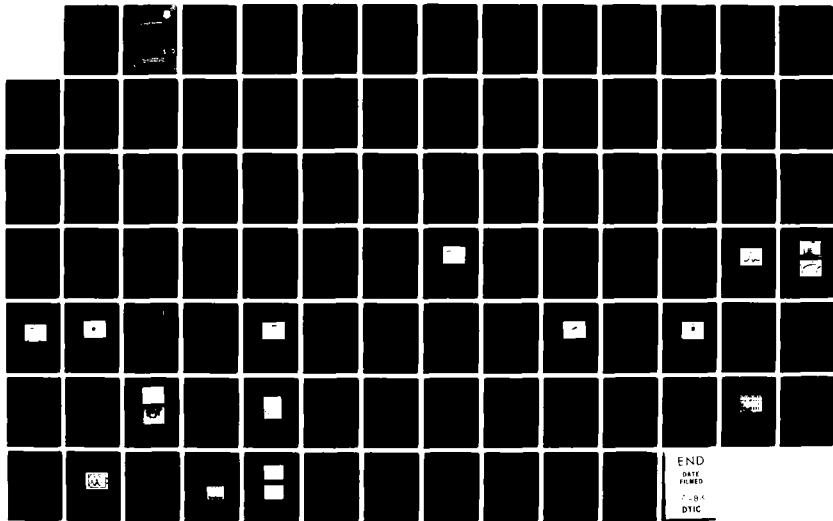
1/1

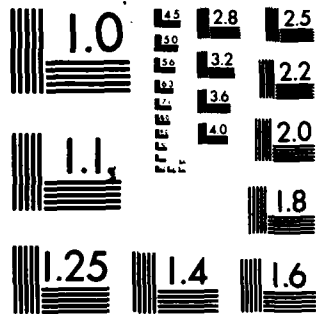
UNCLASSIFIED

F19628-79-C-0143

F/G 17/5

NL





MICROCOPY RESOLUTION TEST CHART
NATIONAL BUREAU OF STANDARDS-1963-A

AD A 129277

127

1

111

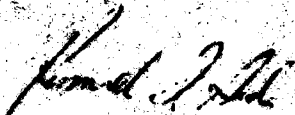
111

111

This report has been reviewed by the RADC Public Release Office and is releasable to the National Technical Information Service (NTIS). It will be releasable to the general public, including foreign countries.

RADC-TR-83-66 has been reviewed and is approved for publication.

APPROVED:



KENNETH J. SODA, Captain, USAF
Project Engineer

APPROVED:



HAROLD ROTH, Director
Solid State Sciences Division

FOR THE COMMANDER:



JOHN P. HUSS
Acting Chief, Plans Office

If your address has changed or if you wish to be removed from the RADC mailing list, or if the addressee is no longer employed by your organization, please notify RADC (RSC) Hanscom AFB MA 01731. This will assist us in maintaining a current mailing list.

Do not return copies of this report unless contractual obligations or conditions on a specific document require that it be returned.

UNCLASSIFIED

SECURITY CLASSIFICATION OF THIS PAGE (When Data Entered)

REPORT DOCUMENTATION PAGE		READ INSTRUCTIONS BEFORE COMPLETING FORM
1. REPORT NUMBER RADC-TR-83-66	2. GOVT ACCESSION NO. AD-4129 277	3. RECIPIENT'S CATALOG NUMBER
4. TITLE (and Subtitle) 1.27 μ m RECEIVER DEVELOPMENT	5. TYPE OF REPORT & PERIOD COVERED Final Technical Report 18 Jun 79 - 17 Jun 80	
	6. PERFORMING ORG. REPORT NUMBER MRDC41031.5FR	
7. AUTHOR(s) H. D. Law P. D. Dapkus K. Nakano	8. CONTRACT OR GRANT NUMBER(s) F19628-79-C-0143	
9. PERFORMING ORGANIZATION NAME AND ADDRESS Rockwell International/MRDC 1049 Camino Dos Rios Thousand Oaks CA 91360	10. PROGRAM ELEMENT, PROJECT, TASK AREA & WORK UNIT NUMBERS 62702F/61102F 46001930/2306J203	
11. CONTROLLING OFFICE NAME AND ADDRESS Rome Air Development Center (ESO) Hanscom AFB MA 01731	12. REPORT DATE March 1983	
	13. NUMBER OF PAGES 82	
14. MONITORING AGENCY NAME & ADDRESS (if different from Controlling Office) Same	15. SECURITY CLASS. (of this report) UNCLASSIFIED	
	15a. DECLASSIFICATION/DOWNGRADING SCHEDULE N/A	
16. DISTRIBUTION STATEMENT (of this Report) Approved for public release; distribution unlimited.		
17. DISTRIBUTION STATEMENT (of the abstract entered in Block 20, if different from Report) Same		
18. SUPPLEMENTARY NOTES RADC Project Engineer: Kenneth J. Soda, Captain, USAF (ESO)		
19. KEY WORDS (Continue on reverse side if necessary and identify by block number) Schottky barrier avalanche photodiode, GaAlAsSb/GaSb material development, heterostructure, ion implanted, hole injection, bandgap-lattice constant, III-V semiconductors, mesa structure, planar structure, liquid phase epitaxy (LPE), quantum efficiency, raster scan, integrated optical receiver, probe set-up, MESFET transimpedance amplifier, epilayer (Cont'd)		
20. ABSTRACT (Continue on reverse side if necessary and identify by block number) This program addressed performance improvements of GaAlAsSb avalanche photo-diodes and low noise GaAs MESFET transimpedance amplifier for 1.3 μ m fiber optic hybrid receiver applications. Although material non-uniformity and device surface leakage problems require further work, GaAlAsSb is a most attractive lattice-matched 1.3 to 1.55 μ m APD material with high gains, quantum efficiencies, and speeds exhibited in a variety of device structures. The GaAs monolithic preamplifier investigated in the		

DD FORM 1 JAN 73 1473

EDITION OF 1 NOV 68 IS OBSOLETE

UNCLASSIFIED

SECURITY CLASSIFICATION OF THIS PAGE (When Data Entered)

UNCLASSIFIED

SECURITY CLASSIFICATION OF THIS PAGE(When Data Entered)

Block 19 (Cont'd)

substrate, hybrid.

Block 20 (Cont'd)

program, capable of frequency operation in excess of 1 GHz with appropriate transimpedance, is an ideal front end for a fiber optic communication receiver or an APD array.

UNCLASSIFIED

SECURITY CLASSIFICATION OF THIS PAGE(When Data Entered)

TABLE OF CONTENTS

	<u>Page</u>
1.0 INTRODUCTION.....	1
1.1 Introduction.....	1
2.0 PROGRAM GOALS.....	4
3.0 TECHNICAL APPROACH.....	5
3.1 Materials Consideration.....	5
3.2 Device Designs and Considerations.....	8
3.3 Receiver Design Considerations.....	16
4.0 TECHNICAL PROGRESS.....	23
4.1 GaAlAsSb/GaSb Material Development.....	23
4.1.1 GaAlSb Materials Growth.....	23
4.1.2 GaAlAsSb Materials Growth.....	29
4.2 Heterostructure Avalanche Photodiode Development.....	37
4.3 Ion Implanted GaAlAsSb Avalanche Photodiode.....	50
4.4 Hole Injection Avalanche Photodiode.....	53
4.5 Schottky Barrier Avalanche Photodiodes.....	57
4.6 GaAlAsSb APD Leakage Study.....	62
4.7 Receiver Fabrication and Testing.....	65
5.0 CONCLUSIONS AND RECOMMENDATIONS.....	81

Accession For	
NTIS GRA&I	<input checked="" type="checkbox"/>
DTIC TAB	<input type="checkbox"/>
Unannounced	<input type="checkbox"/>
Justification	<input type="checkbox"/>
By _____	
Distribution/ _____	
Availability Codes	
Dist	Avail and/or Special
A	



LIST OF FIGURES

3.1	Bandgap-lattice constant vs composition diagram for alloys of III-V semiconductors.....	6
3.2	1.0-1.4 μm GaAlAsSb APD.....	9
3.3	Schematic cross section of 1.3 μm ion implanted APD. (a) Mesa structure, (b) planar structure.....	10
3.4	Hole injection structure.....	13
3.5	An illustration of edge breakdown caused by $N_A > N_D$. Because of the equal area rule, the peak field at the edge is higher than the peak field inside the bulk.....	15
3.6	30 MHz receiver block diagram arrangement.....	18
3.7	Model used for analysis of signal and noise response. e_1 is the equivalent input noise voltage generator of the preamp, e_2 is the Johnson noise voltage generator of the conductance G_F . In (b), G_I replaces the input conductance of the preamp and the conductance of the APD and i_{nj} replaces e_2	20
4.1	Typical LPE growth schedule (see text).....	26
4.2	Arsenic liquidus in a gallium melt vs arsenic mole fraction in the solid.....	30
4.3	X-ray rocking curve of a GaAlAsSb epitaxial layer lattice matched to within 0.012% to GaSb.....	32
4.4	Lattice mismatch as a function of arsenic in the liquidus (atomic fraction).....	34

LIST OF FIGURES

<u>Figure</u>		<u>Page</u>
4.5	Lattice mismatch as a function of arsenic in the liquidus at high Al content.....	35
4.6	Typical reverse characteristic of a GaAlAsSb APD.....	38
4.7	Capacitance-voltage and doping profile of a GaAlAsSb heterojunction APD.....	40
4.8	Photoresponse of a GaAlAsSb heterojunction APD.....	41
4.9	Photograph of the speed of response of a GaAlAsSb heterojunction APD.....	43
4.10	The speed of response of a GaAlAsSb APD with absorption occurring (a) in the active layer; (b) in the window layer.....	44
4.11	Photograph of the uniform gain possible with a GaAlAsSb APD.....	45
4.12	Photoresponse intensity modulated scan of a GaAlAsSb heterojunction APD.....	46
4.13	Plot of microwave gain vs voltage of the best Be-implanted GaAlAs APD.....	47
4.14	Reverse I-V characteristic demonstrating the effect of high surface leakage.....	49
4.15	External quantum efficiency vs wavelength of a Be-implanted GaAlAsSb avalanche photodiode without antireflection coating.....	52

LIST OF FIGURES

<u>Figure</u>		<u>Page</u>
4.16	Reverse I-V characteristic of a Be-implanted GaAsAsSb homojunction APD.....	54
4.17	Gain vs bias voltage of a Be-implanted GaAlAsSb homojunction APD.....	55
4.18	Intensity modulated scan of an ion implanted GaAlAsSb APD at 273 MHz and gain of 90; showing uniformity of gain over entire optical area to 10%.....	56
4.19	Photoresponse of the hole injection GaAlAsSb photodiode with too thick a window layer.....	58
4.20	Gain vs voltage of a hole injection GaAlAsSb photodiode.....	59
4.21	Photoresponse profile of a Schottky barrier APD at (a) zero bias; (b) 20 V reverse bias.....	61
4.22	Raster scan of a Schottky barrier GaAlAsSb diode with an inverted surface.....	63
4.23	The forward I-V characteristics of a GaAlAsSb APD at various temperatures.....	66
4.24	The reverse characteristics of a GaAlAs Sb APD at various temperatures.....	67
4.25	Schematic diagram of photodiode preamplifier.....	68
4.26	Cut-a-way view showing two planar diodes and a planar FET and their interconnections.....	69

LIST OF FIGURES

<u>Figure</u>		<u>Page</u>
4.27	Integrated optical receiver encircled by box.....	71
4.28	Schematic diagram of (a) probe set-up and (b) measurement technique for obtaining C_c	73
4.29	Input and output voltages for first stage of preamplifier when a 100 K Ω input resistor is used.....	74
4.30	(a) Schematic representation of relative preamp response vs frequency when capacitatively coupled (b) Actual response of GaAs IC preamplifier.....	76
4.31	Frequency response of capacitatively coupled GaAs preamp under different bias condition than Fig. 4.30.....	77
4.32	Plot of NEP vs frequency.....	80

LIST OF TABLES

<u>Table</u>		<u>Page</u>
4.1	Data on 450°C GaAlSb Growth.....	27
4.2	Data on 500°C GaAlSb Growth.....	28
4.3	Data on 475°C GaAlSb Growth.....	28
4.4	Data on 400°C GaAlSb Growth.....	29
4.5	Data on 500°C GaAlAsSb Growth.....	33
4.6	Estimated Junction Depths of Different Implant Energy and Dosage of Be; After 450°C, 10 min Annealing; The Background is Assumed to be $1 \times 10^{16} \text{ cm}^{-3}$	51
4.7	Surface Treatments on GaAlAsSb.....	64
4.8	Dielectric Coatings on GaAlAsSb.....	64

1.0 INTRODUCTION

1.1 Introduction

The rapid development of optical fibers with extremely low loss (<0.5 dB/Km) and near zero wavelength dispersion in the $1.25 \mu\text{m}$ to $1.30 \mu\text{m}$ wavelength range have led to a search for suitable high performance semiconductor lasers and avalanche photodetectors in this wavelength range. Realization of the ultimate potential of fiber optics in general requires the development of extremely sensitive, high speed optical receivers. Over the past several years, efforts to develop direct energy bandgap III-V alloy materials suitable for use in the $1-2 \mu\text{m}$ region have demonstrated the tremendous device potential of these materials. The quality and availability of these materials, however, continue to limit device performance and, therefore, system applications.

In order to fully exploit the capabilities of present optical fiber technology, the photodetector used in the optical receiver must have the following properties:

1. High quantum efficiency
2. High speed impulse response
3. Moderate avalanche gain
4. Low dark current
5. Low capacitance.

It is obvious that at present no single material system meets all five criteria. The further development of a given material system should be based on demonstrated device performance. A research program should determine whether the limiting factors can be removed by further materials improvement or whether there are intrinsic limitations of the particular material system. The program described in this report was directed at improving the performance of GaAlAsSb avalanche photodiodes and demonstrating this in concert with a low noise GaAs MESFET transimpedance amplifier.

Several reasons for this approach are evident. The low quantum efficiency of silicon (for $\lambda > 1 \mu\text{m}$) and high dark current of Ge are inherent to the materials and cannot be eliminated by further technology development. The poor uniformity of optical response under avalanche conditions of GaAsSb and InGaAs is a result of poor epilayer-substrate lattice matches, which is inherent to the material systems and probably can never be completely eliminated. Recent 1.0-1.4 μm detector work has concentrated on the attainment of high quantum efficiency, avalanche gain in two lattice matched III-V alloy systems suitable for optimum fiber optical wavelength range (1.0-1.4 μm): GaAlAsSb and InGaAsP. Rockwell's intensive experience with the GaAlAsSb system and excellent early performance results dictated its choice.

Rockwell has developed 1.0-1.4 μm avalanche detectors and has demonstrated the ability to hybrid integrate avalanche photodetectors with ultra-high speed GaAs MESFETs in a circuit design that results in an optical receiver with a 50 to 100 times lower noise equivalent power than is possible with conventional techniques.

The effort described below will detail the further development of 1.3 μm GaAlAsSb detectors, the development of monolithic GaAs integrated circuit optical receivers, and the verification of their performance by testing.

This report is divided in the following way. Section 2.0 outlines the program objectives and goals. Section 3.0 outlines the general technical approach. The details of the technical progress are outlined in Section 4.0, and conclusions based on this work as well as recommendations for future work are described in Section 5.0.

2.0 PROGRAM GOALS

The overall objective of this program was to develop a high performance GaAlAsSb avalanche photodiode sensitive to 1.3 μm radiation and a 0-100 MHz low noise transimpedance amplifier-receiver for use with this photodiode in fiber optics systems.

The specific device and receiver performance goals are as follows:

Avalanche Photodiode

Wavelength Cutoff	1.3 μm
Impulse Response	<120 ps
Quantum Efficiency	>90%
Avalanche Gain	30%
Gain Uniformity	$\pm 10\%$
Active Element Size	100 μm ϕ
Dark Current	~ 1 nA

Optical Receiver

Bandwidth	0-100 MHz
NEP	10^{-9} W/ $\sqrt{\text{Hz}}$ (0-100 MHz)

One detector in a high frequency package and one 0-100 MHz optical receiver with OSM connectors were to be delivered to RADC at the end of the contract.

Section 4.0 shows that significant progress towards reaching these goals was made in this program.

3.0 TECHNICAL APPROACH

The construction of a low noise avalanche photodiode receiver at 1.3 μm requires careful selection of the materials, device design, and receiver design to achieve the required 100 MHz bandwidth and high performance optical devices. The following sections will describe the considerations for choice of materials as well as the device and receiver design to achieve the goals of this program.

3.1 Materials Consideration

The GaAlAsSb materials system is a unique quaternary system for the fabrication of materials suitable for 1.3 μm devices. It is similar to the GaAlAs ternary materials system in that the bandgap of a particular composition can be increased with very small change in the lattice constant merely by increasing the Al to Ga ratio. This is illustrated in Fig. 3.1 by the bandgap vs lattice constant diagram of the GaAlAsSb material system. Note that both of the composition lines designed by the GaAlAs and the GaAlSb material systems are almost vertical. This means that it is possible to grow lattice matched materials over a wide bandgap range to both GaAs and GaSb substrates. In the case of GaSb, the bandgap of the GaAlSb materials system can be varied from 0.7 eV to ~ 1.6 eV merely by changing the Ga to Al ratio. Perfect lattice matching of the alloy to the GaSb substrate can be achieved by adding small amounts of As while maintaining the Ga to Al ratio. For example, in the highest bandgap material only 7% As is required in the lattice to achieve

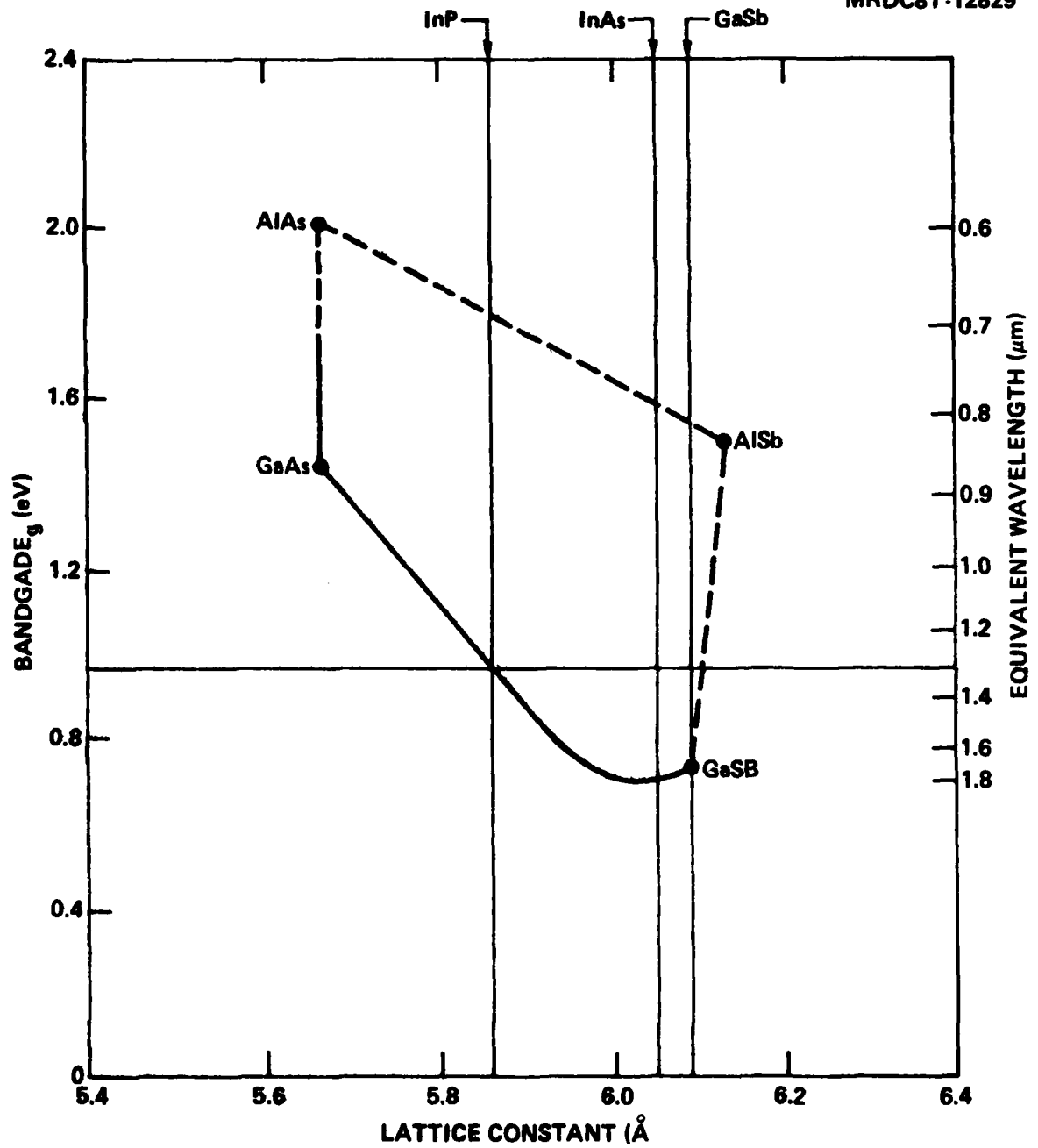


Fig. 3.1 Bandgap-lattice constant vs composition diagram for alloys of III-V semiconductors.

lattice matching to the GaSb substrate. Similarly, the lattice constant of the material can be varied over the range from GaAs to GaSb by changing the As to Sb ratio. Thus, it is possible, for example, to lattice match a GaAlAsSb layer to an InAs substrate by the inclusion of ~ 10% of As to a GaSb wafer. The lattice matching point to InP is about equal concentrations of As and Sb. This material system gives a great deal of flexibility for the fabrication of avalanche photodiodes. When utilizing GaSb substrates, the active region of a 1.3 μm device is grown with approximately 20% Al in the solid. At this composition, only 2% of As in the solid is required. To grow a window layer transmitting 1 μm radiation on this active layer requires the growth of a $\text{Ga}_{0.5}\text{Al}_{0.5}\text{Sb}$ layer, and this layer requires ~ 4% As in the solid. As will be shown later, the solubility of As in Ga melts at a temperature suitable for growing Sb rich solids is quite low. As a result, achieving lattice matched conditions to a GaSb substrate for lightly doped active regions is not possible beyond a wavelength of 1.3 μm . Thus, the ideal composition for an active region for a 1.3 μm device is ~ $\text{Ga}_{0.8}\text{Al}_{0.2}\text{As}_{0.3}\text{Sb}_{0.97}$.

The growth of GaAlAsSb on either InAs or InP substrates would be difficult by liquid phase epitaxy for two reasons. First, both substrates are quite dissimilar from the melt constituents used to grow the GaAlAsSb, and dissolution of the substrate prior to the initiation of the growth is possible. Secondly, both substrates have relatively high vapor pressures of the column V element below their melting points which could serve to contaminate GaSb melts, the third, and perhaps most important, at the temperatures at which the material is to be grown (~ 500°), the solubility of As in a Ga melt

is quite low, and thus achieving solid composition with sufficient As to be lattice matched to either InAs or InP substrates is not possible. In this respect, it would be most advantageous to grow these compounds by metallorganic chemical vapor deposition where an arbitrary composition can be achieved by appropriate gas phase compositional control.

3.2 Device Designs and Considerations

Four different device designs were considered during this program for 1.3 μm avalanche photodiodes. The first and most likely high performance design was the heterostructure avalanche photodiode design shown schematically in Fig. 3.2. Here, a lightly doped active region is grown directly on the substrate followed by the growth of a larger bandgap window layer which is heavily doped. The heavy doping of the window layer provides the conductivity necessary for contacting, and it ensures that the depletion width is totally contained in the active region. For active region doping below 10^{16} and for appropriately doped window layers, absorption occurs in the active region entirely within the depletion depth. Carriers are then collected by being swept by the built-in field of the junction directly to the heterojunction. This ensures both high quantum efficiency (no surface recombination and no diffusion loss) and high speed (no diffusion tail). In most respects, this device design is optimum for APD performance in every respect except the excess avalanche noise, since it will suffer from mixed carrier generation.

The ion implanted homojunction avalanche photodiode is shown schematically in Fig. 3.3. Here, the p-n junction is formed by ion

MRDC81-12831

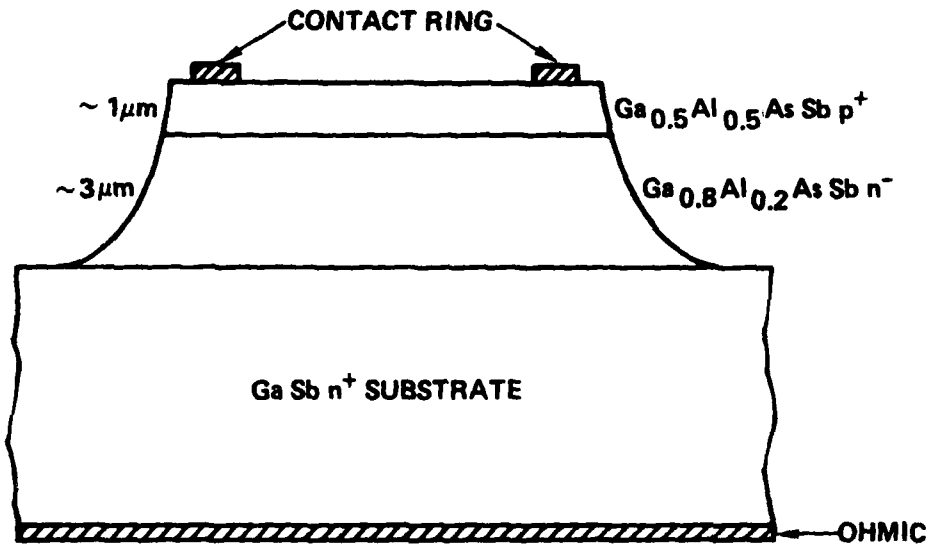
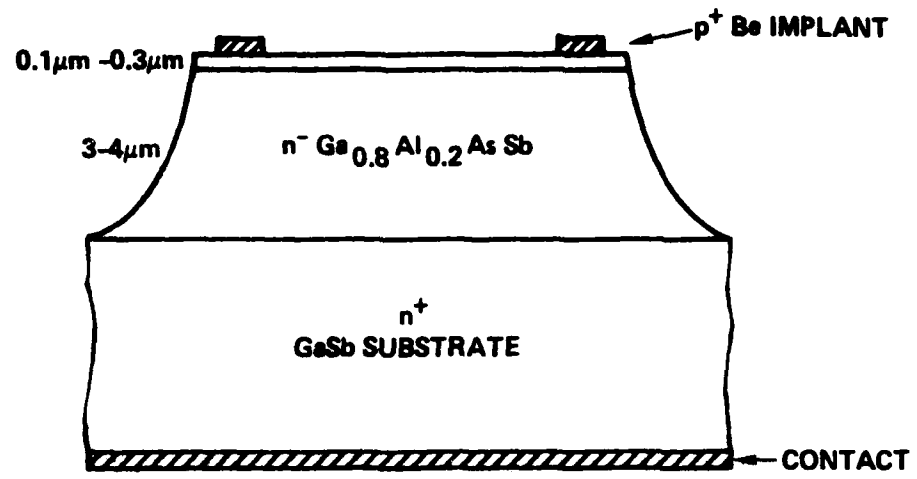
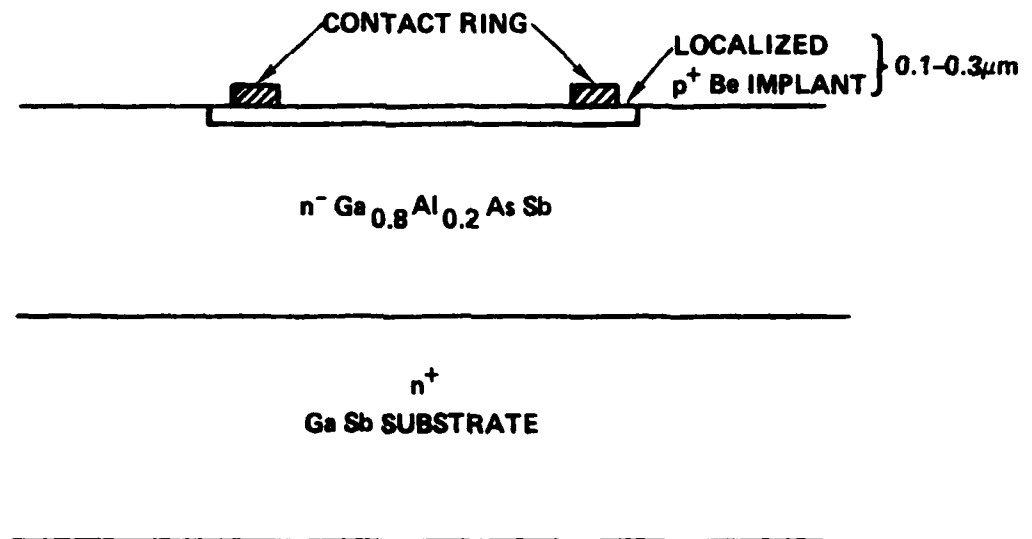


Fig. 3.2 1.0 to 1.4 μm GaAlAsSb APD.



(a)



(b)

Fig. 3.3 Schematic cross section of 1.3 μ m ion implanted APD.
 (a) mesa structure; (b) planar structure.

implantation of Be atoms directly into the surface of a lightly doped epitaxial layer. The performance of this device is critically dependent upon a high quality Be implant, a shallow implantation profile to minimize surface losses and carrier diffusion effects, and high quality material. The planar ion implanted structure shown in Fig. 3.3b requires a surface passivation technique to reduce the surface current leakage owing to the penetration of the implanted junction at the top surface of the wafer. In addition, some means to reduce the field gradients at the curved portion of the implanted junction is also required. Our initial device structures have obviated these two problems by the use of the device structure shown in Fig. 3.3a which is a mesa device design. The homojunction design will inevitably have absorption within the p region of the detector. If this region is heavily enough doped to be undepleted, collection of carriers from it will require diffusion to depletion region and the p-n junction. This inevitably will slow the device down compared to a heterostructure avalanche photodiode and may limit the quantum efficiency of the device if surface recombination velocity of the material is high.

Preliminary ionization rate data show that holes in the GaAlAsSb compounds are better ionizers than electrons. The excess avalanche noise depends on the ionization rate difference and the injection methods. If one injects the carriers with the higher ionization rate, one will get a lower multiplication noise. In fact, the excess noise term can be written as:

$$\overline{i_{en}^2} = 2qB(I_d + I_{ph})M^2F$$

where, i_{en} is the excess noise current; B , the bandwidth; I_d , the dark current of the diode; I_{ph} , the average photocurrent; M , the multiplication factor; and F , the excess noise factor. For $\alpha = \beta$, the excess noise factor is close to M . On the other hand, if $\alpha \gg \beta$, and the diode is designed to have electron injection, F tends to unity. However, if $\alpha \gg \beta$, and the diode is designed to have hole injection, F tends to M^2 . From similar analysis, the converse is true for $\beta \gg \alpha$ also. Therefore, we should design the GaAlAsSb diode to have the hole injection. Traditionally, the highest performance diode will have p^+n structure with the window layer on top. This structure will create electron injection. A complementary structure n^+p diode will have the right injection method. Although high purity p type GaAlSb materials have been grown, the controllability is not as good as the Te doped n type material. Also, we anticipate problems in making good ohmic contacts on n type GaAlSb with high percentage of aluminum. Therefore, a different structure was designed to have the hole injection. The structure is shown in Fig. 3.4. The junction is inside the window layer. When the photons enter the diode, they will be absorbed in the absorption layer. The holes generated will drift back towards the window layer. To have the right operation condition, the distance from the electrical junction to the metallurgical junction between the absorption and the window layer is very critical. If this distance is too long, at operating point, the depletion region does not punch through to the absorption

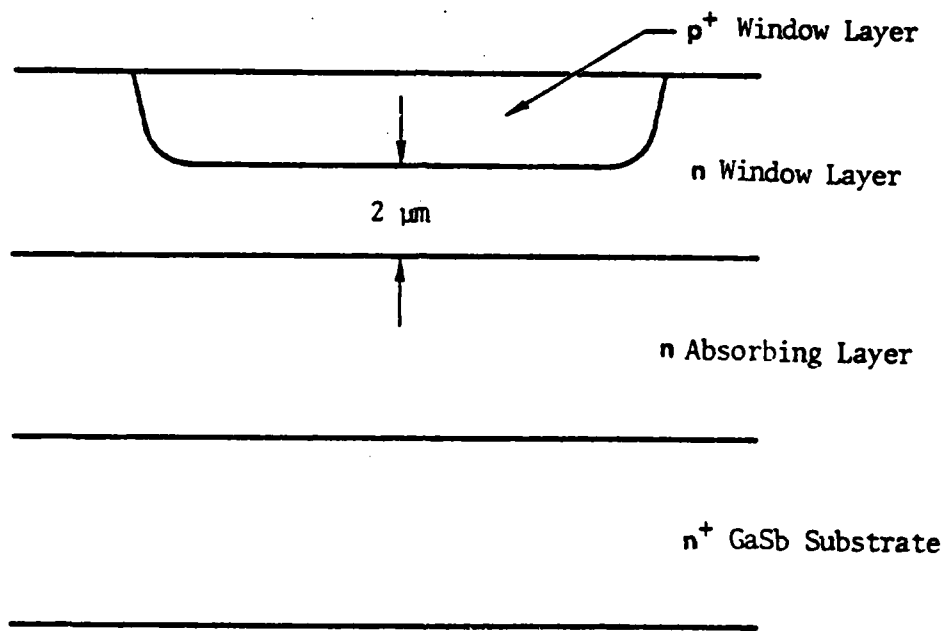


Fig. 3.4 Hole injection structure.

region. The generated holes have to rely on the diffusion process which is further obstructed by the high heterojunction barrier that the holes have to climb up. Consequently, the quantum efficiency will be very low, and the speed of the diode will be slow. On the other hand, if the distance between the electrical junction and the metallurgical junction is too short, the injection of holes will not be pure. The electrical field extends too far out to the absorption region, and the generated electrons will have a chance to multiply. The ideal device is that the electric field extends to one fifth of its region into the absorption region at operating point. In such cases, the quantum efficiency will still be high while the carrier injection is relatively pure.

The detailed technical difficulties in the structure as shown in Fig. 3.4 are not trivial. There are several important criteria to make this structure work. The n type doping of the window layer has to be lower than the absorbing layer. If the reverse is true, the lateral field inside the window layer will be higher than the perpendicular field as illustrated in Fig. 3.5. Depending on the difference in doping, breakdowns are likely to happen at the perimeter of the diode. (The ionization rates in the window layer and the absorbing layer are not known quantitatively at this moment. The fact that the ionization rates are likely to be lower in wider bandgap material will make this problem less critical. However, the doping in the window layer cannot be much higher than the absorbing layer.) Also, as mentioned above, the distance of the electrical junction and the metallurgical junction between the absorbing layer and the window layer is critical. This

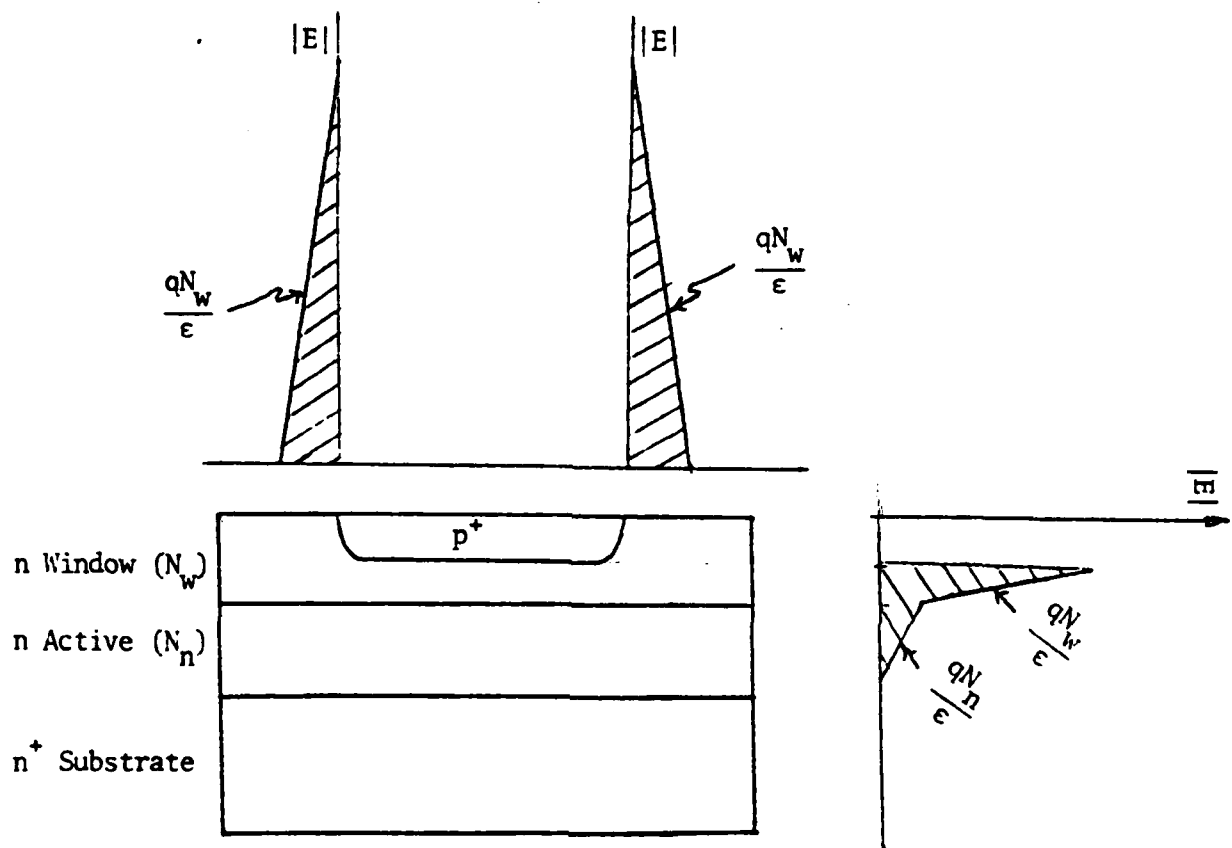


Fig. 3.5 An illustration of edge breakdown caused by $N_w > N_n$. Because of the equal area rule, the peak field at the edge is higher than the peak field inside the bulk.

will require a great deal of control in the uniformity of the epitaxial layer, the diffusion rate (in the case of diffused junction), and the implant depth of the Be ions.

The final design considered in this program was a Schottky barrier APD. This also is quite simple to fabricate like the homojunction APD. Here, it will be difficult to maintain the efficiency of the other device designs owing to the need to have a Schottky metallization for carrier collection. While this may be maintained for relatively small metal layer thicknesses, there will be some absorption in the Schottky barrier layer which in turn will limit the quantum efficiency of the device. In addition, the I-V characteristics of these devices are uniquely dependent upon the surface characteristics of the material.

3.3 Receiver Design Considerations

To successfully achieve a high performance 30 MHz APD receiver as outlined in the goals of this program, it is necessary to develop a low noise high performance amplifier to be used in concert with the photodiodes described in the previous section. The efforts in this phase of the program were devoted to developing a 100 MHz bandwidth transimpedance amplifier. Considerable development of low noise transimpedance preamplifiers has been undertaken under a variety of programs for both the Air Force and NASA. In this program, the amplifier supplied and delivered on contract deviated significantly from our previous efforts. While all of the others were hybrid integrated amplifiers, the preamp described in this section was a monolithic GaAs

integrated circuit preamplifier. The design of this preamplifier was based on work done in previous programs on the hybrid structures and utilizes all of the design criterion developed in this work.

The 100 MHz transimpedance preamplifier design utilized for this program is one based on a previous design by R.C. Eden and incorporated into fabrication masks for GaAs ICs. A schematic diagram of the preamp is shown in Fig. 3.6. Also shown in 3.6 is a block diagram model of the preamplifier components. As can be seen, the preamplifier consists of two major sections, a transimpedance amplifier consisting of amplifiers A_1 and A_0 and a current amplifier A_2 . When A_1 and A_0 are configured with a feedback resistor such as shown in the diagram, the amplifier combination is a transimpedance amplifier. So long as the gain of this combination is high ($A_1 \times A_0 \gg 1$), the output voltage of the combination is approximately equal to $V_f = I_p \times R_f$. The major requirements for such a preamplifier are the following: (1) The loop frequency response of the amplifier ($A_1 \times A_0$) must be greater than the overall closed loop bandwidth of 100 MHz. (2) The input capacitance is composed of the photodiode capacitance, the input capacitance of the preamplifier, and the stray capacitance are of primary importance to the frequency response and the noise performance of the amplifier. As a result, the input capacitance must be as small as possible. Similarly, in order to reduce the noise current generated by the feedback resistor and the first stage amplifier, it is necessary to maximize the feedback resistance R_f . (3) The ultimate closed loop frequency response is limited by the stray capacitance shunting the

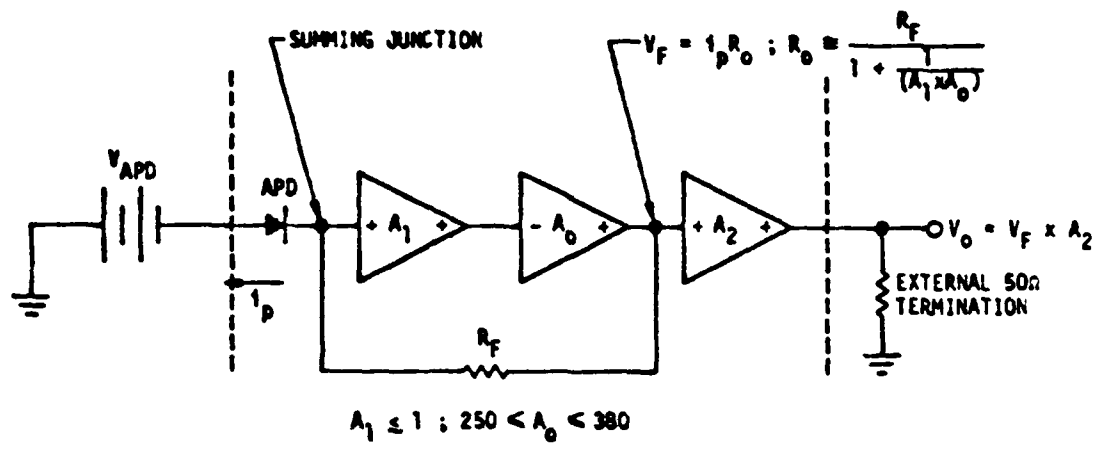


Fig. 3.6 30 MHz receiver block diagram arrangement.

feedback resistor. This must be minimized. These three criteria must be satisfied in order to achieve optimal performance from the preamplifier.

The amplifier A_2 is a current amplifier designed to isolate the output of A_0 from the capacitance loading and to enable the receiver to drive 50 ohm lines. In the receiver characterized here and delivered to RADC, this stage had a voltage gain of 0.95.

The voltage gain section A_0 must have extremely high gain bandwidth product, so as not to introduce additional phase shift in the 100 Hz pass band. Only then is the advantage of the high effective load resistance and the resulting lower noise performance of the transimpedance amplifier realized.

The input amplifier A_1 must exhibit low equivalent input voltage noise spectral density and very low input capacitance. Since the amplifier noise is proportional to E_n and C_i , we believe that to first order the contribution of these elements is somewhat interchangeable. The resistance element R_f must be designed to have minimal shunt capacitance and minimal feed through capacitance.

A reasonable model for the receiver for both signal and noise successfully applied to hybrid amplifiers in other programs is represented in Fig. 3.7. Figure 3.7a is the generalized model with e_1 and e_2 being frequency dependent voltage noise sources of the amplifier and of the feedback element G_f , respectively. The amplifier $A(\omega)$ is considered to have infinite input

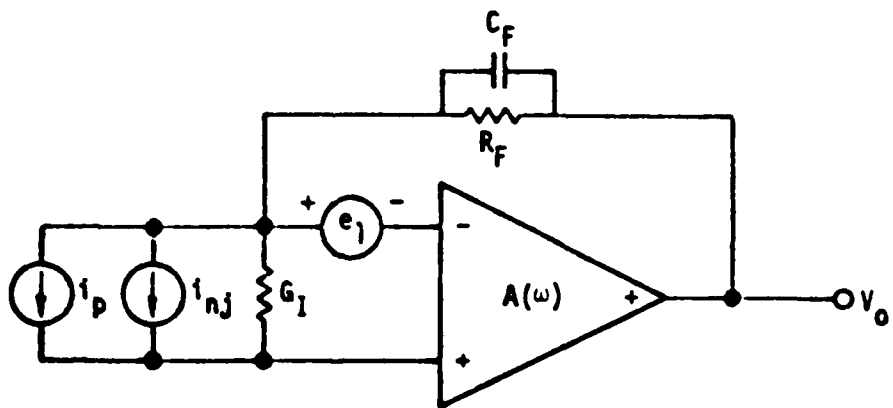
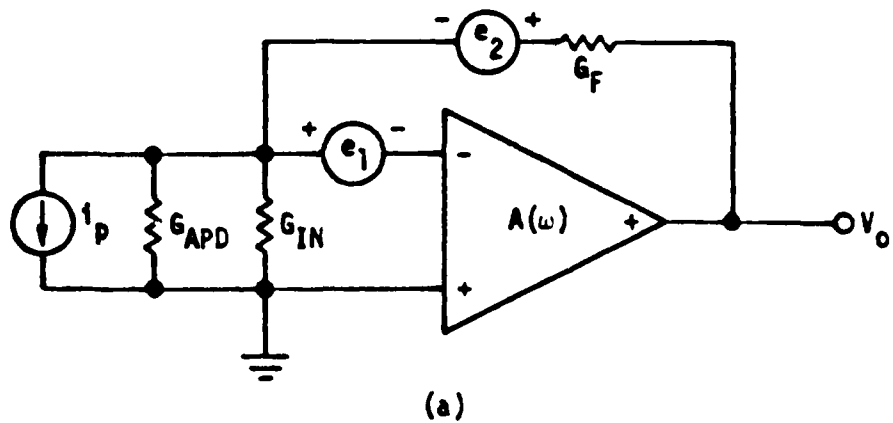


Fig. 3.7 Model used for analysis of signal and noise response. e_1 is the equivalent input noise voltage generator of the preamp, e_2 is the Johnson noise voltage generator of the conductance G_F . In (b), G_I replaces the input conductance of the preamp and the conductance of the APD and i_{nj} replaces e_2 .

impedance, zero output impedance and zero noise. Its frequency dependence is taken to be:

$$A(\omega) = \frac{A_0}{1 + j \frac{\omega}{\omega_A}}$$

where A_0 is the low frequency gain, and ω_A is the amplifier 3 db frequency. This model is drawn more explicitly in Fig. 3.5b where G_F is modeled with R_F in parallel with C_F , and e_2 , the Johnson noise voltage term, is converted to its equivalent frequency impedance current form and indicated in parallel with I_p at the input of the amplifier.

G_{IN} for the devices used in the input stage is virtually purely capacitive, as is G_{ARD} , so that their combination, G_I , in Fig. 3.5b is considered as a capacitance in the analysis. The forward transimpedance for this model is given by:

$$V_o = \frac{(i_p + i_{nj}) \left(\frac{1}{G_F} \right)}{1 + \frac{1}{A} \left(1 + \frac{G_I}{G_F} \right)} + \frac{e_o (G_F + G_I)}{G_F + \frac{1}{A} (G_F + G_I)}$$

where $i_{nj} = \frac{4kt}{R_F} \text{ Amps}/\sqrt{\text{Hz}}$,

$$G_I = j\omega C_I, \quad G_F = \frac{1}{R_F} + j\omega C_F$$

$$A = \frac{A_0}{1 + \left(\frac{\omega}{\omega_A}\right)^2}$$

Note that in the ideal case of zero noise, zero input conductance, and zero C_F ,

$$V_o = \frac{i_p R_F}{1 + \frac{1}{A}} \equiv i_p R_o$$

In principle, this model could be used to calculate the expected frequency response of the amplifier as well as the noise performance.

4.0 TECHNICAL PROGRESS

This section describes the technical progress achieved in the development of materials, the fabrication and testing of device structures and the fabrication and testing of the 100 MHz receiver.

4.1 GaAlAsSb/GaSb Material Development

The GaAlSb/GaSb ternary alloy system is similar to the GaAlAs/GaAs ternary system. The addition of the aluminum increases the bandgap of the alloy while its lattice constant does not change much from that of the GaSb substrate. In fact, the percentage change in the lattice constant, $\Delta a/a_0$, between AlSb and GaSb is only 0.7%. In the optoelectronics devices, for the wavelength range of interest (0.96 μm to 1.8 μm), the highest aluminum antimonide content alloy needed is 50%. In other words, the maximum lattice mismatch is 0.35%. By adding in a slight amount of arsenic, the lattice constant of the quaternary GaAlAsSb can be made lattice matched to the GaSb. Only 3.5% of arsenic is required to lattice match a 50% AlSb alloy.

4.1.1 GaAlSb Materials Growth

The quaternary GaAlAsSb alloys require a growth temperature near 550°C to dissolve enough arsenic in the Ga melt to achieve lattice matching. The ternary GaAlSb, however, can be grown at temperatures as low as 400°C. The p-type background doping of the antimonide materials is thought to be due to antimony vacancies. The concentration of antimony vacancies depend on the

growth rate of the crystal. A slow growth rate reduces the concentration of antimony vacancies. This is the motivation of growing the crystal at a lower temperature where the growth rate is lower. At a growth temperature of 500°C, undoped GaAlSb crystals were p-type. At a growth temperature of 450°C, undoped crystals were n-type. To prove that this effect was not due to amphoteric dopants, a layer was grown at 450°C at a ramping rate of 0.5°C/min. After the initial growth, we moved the melt such that it covered only half of the substrate and increased the ramping rate to 5°C/min. A hot point probe was used to determine the type of doping of the growth. It was found that the growth with a slow ramping rate was n-type while the growth with a fast ramping rate was p-type, although they were both grown with the same melt.

The lattice mismatch of a ternary GaAlSb epitaxial film with a GaSb substrate is a problem for high performance detectors at 1.3 μm . However, for longer wavelength operation such as 1.55 μm , the lattice mismatch is very small. With the increasing interest in systems operating at 1.55 μm , the ternary GaAlSb crystal growth at low temperature should be investigated. Although the ternary GaAlSb may not be suitable for short wavelength detectors, it is useful for longer wavelength detectors ($\lambda > 1.5 \mu\text{m}$).

The GaSb substrates used in these experiments were either tellurium doped n-type or undoped p-type $\langle 100 \rangle$ material. The etch pit density of the Te doped substrate is approximately 500/cm² while the undoped substrates have EPD of less than 1000. They were chemical-mechanically polished on a "kitten ear" pad with Br-CH₃OH dripping on it. Due to the softness of GaSb, at least 5 mils

of the material was removed by this method to remove saw-induced damage. Some of the samples were polished in fused silica gel to provide a smoother finish. Prior to growth, the substrates were again etched in Br-CH₃OH to remove approximately 1 mil of the material. At times, the etch created a dull surface on the Te doped GaSb substrates. This resulted from the doping striations and did not affect the LPE growth. The Te doped substrates were usually soaked in concentrated H₂SO₄ for 5 minutes to remove any excess Te from the surface. This is especially important for growing high purity material owing to the high distribution coefficient of Te. The substrate was then rinsed thoroughly in deionized water to remove all sulphate ions, followed by an HF soaked to dissolve any residual oxides.

For growing detector quality material in the GaAlSb or GaAlAsSb systems, a long bake of the Ga melt out at high temperature is mandatory. The gallium melt together with the precisely measured antimony and GaAs were baked in purified H₂ atmosphere at 750°C for 12 hours. Figure 4.1 shows a typical growth schedule. Sections A, B and C of the schedule were for baking out the melt. At D, the substrate together with the dopants and aluminum were loaded such that the aluminum was not touching the melt. The furnace was then raised to 600°C for half an hour and the aluminum was mixed with the melt.

The growth schedule for the 450°C GaAlSb is shown in Fig. 4.1. The same bakeout and loading procedures previously described were used. After baking out the melt and loading the substrate, the furnace is raised to 600°C to reduce excess oxide while the aluminum is being mixed. The furnace is then

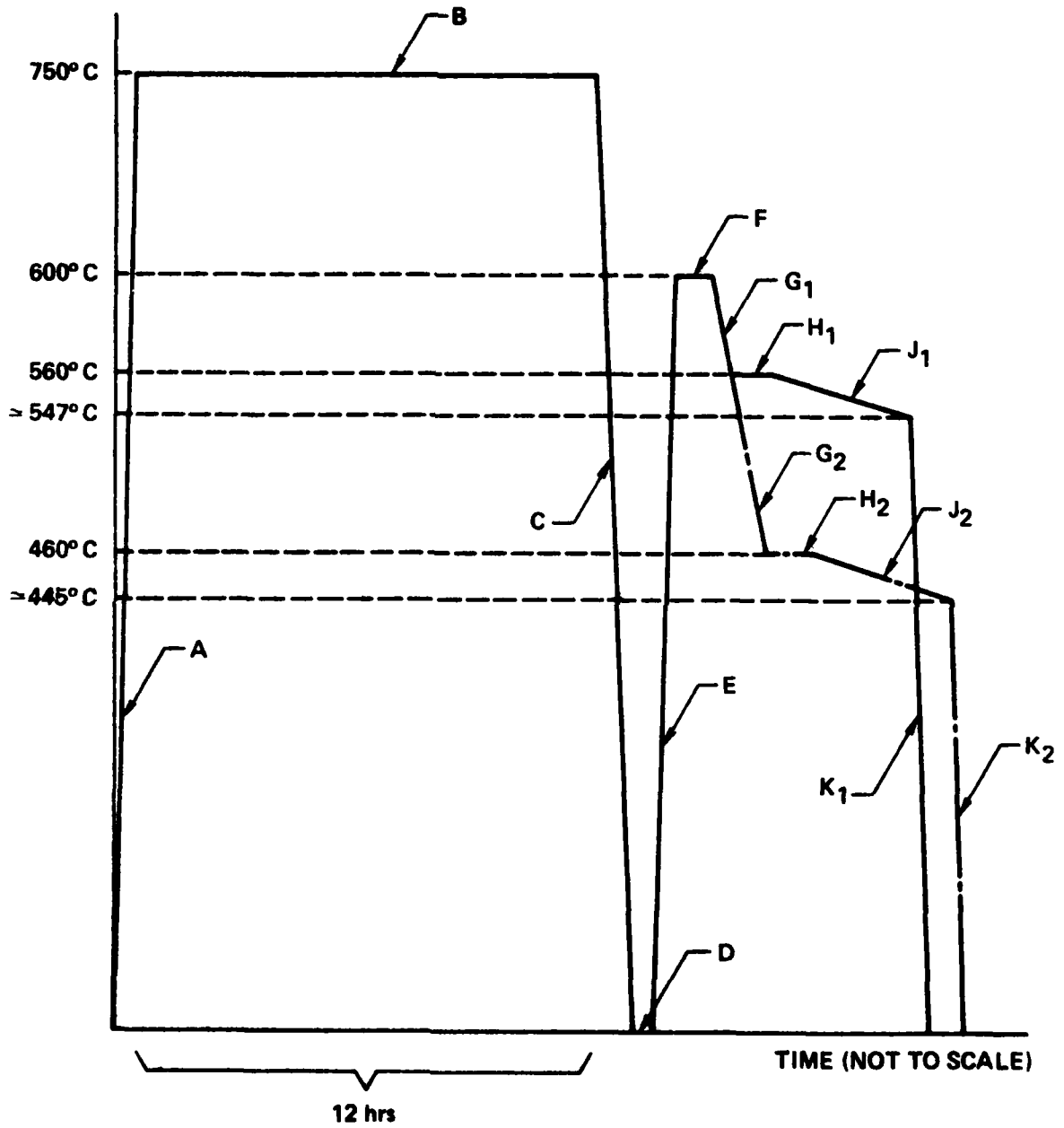


Fig. 4.1 Typical LPE growth schedule (see text).

equalibrated at 460°C and the ramping started. Table 4.1 shows some of the GaAlSb melt data at around 450°C.

Table 4.1
Data on 450°C GaAlSb Growth

x_{Al}^I	x_{Sb}^I	T_{sat} (°C)	T_g (°C)	λ_g (μm)	x of $Ga_{1-x}Al_xSb$
0.0165	0.009	457	452	1.00	0.5
0.013	0.01	456	453	1.09	0.43
0.0082	0.012	457	454	1.18	0.28
0.006	0.013	457	456	1.31	0.2
0.003	0.0155	466	463	1.49	0.11
0.0017	0.015	458	456	1.55	0.06

The growth data for 500°C, 475°C and 400°C are shown in Tables 4.2, 4.3 and 4.4 respectively. The technique used is the same as that used for growth at 450°C.

Table 4.2
Data on 500°C GaAlSb Growth

x_{Al}^I	x_{Sb}^I	T_{sat} (°C)	T_g (°C)	λ_g (μm)	x of $Ga_{1-x}Al_xSb$
0.02161	0.01663	500	498	0.95	0.53 (1)
0.019	0.0165	495	493	1.02	0.48
0.01304	0.0221	504	501.5	1.13	0.30
0.01304	0.0215	502.5	500.5	1.12	0.30
0.0105	0.0232	502	500	1.17	0.28
0.008	0.037	528	524.5	1.31	0.19
0.0075	0.032	517	515	1.29	0.20 (2)
0.0072	0.0236	497	495	-	0.21
0.005	0.0355	520	518	-	0.14
0.0029	0.0315	507	500	1.49 μm	0.08
0.0029	0.0303	504.5	500.5	1.49 μm	0.08
0.0029	0.0294	503	500	1.485 μm	0.08
0.0029	0.029	502.5	500	1.48 μm	0.08
0.002	0.0305	504	501	1.55 μm	0.06
0.002	0.0298	503	500	1.56 μm	0.06

Table 4.3
Data on 475°C GaAlSb Growth

x_{Al}^I	x_{Sb}^I	T_{sat} (°C)	T_g (°C)	λ_g (μm)	x of $Ga_{1-x}Al_xSb$
0.017	0.0125	476	473	0.94	0.51 (1)
0.009	0.016	474	472	-	0.28
0.0065	0.018	479	476	1.31	0.20 (2)
0.006	0.0183	478.5	476	1.43	0.18

(1) Suitable for the window layer of a heterostructure APD.
(2) Suitable for the active layer of a heterostructure APD.

Table 4.4
Data on 400°C GaAlSb Growth

x_{Al}^I	x_{Sb}^I	T_{sat} (°C)	T_g (°C)	λ_g (μm)	x of $Ga_{1-x}Al_xSb$
0.015	0.0042	415.5	412	0.97	0.50
0.015	0.003	398.5	393.5	0.95	0.51
0.01	0.0045	409	405	1.084	0.37 (1)
0.01	0.00382	400	396	1.04	0.35
0.009	0.0035	394	392	-	0.35
0.0053	0.005	406	403	1.265	0.22
0.0045	0.006	412	408	1.33 μm	0.19 (2)
0.0015	0.0055	402	398	1.53 μm	0.06

(1) Suitable for window layer of heterostructure APD.

(2) Suitable for active layer of heterostructure APD.

The surface morphology of a $Ga_{0.72}Al_{0.28}Sb$ crystal grown at 450°C is still reasonably smooth. Rough irregular wavefront-like patterns start to develop on $Ga_{0.5}Al_{0.5}Sb$ crystals grown at the same temperature. X-ray deflectionometer measurements of the $Ga_{0.5}Al_{0.5}Sb$ crystal show broad half widths. It is most probably due to the strain of the lattice mismatch between the substrate and the epitaxial layer.

4.1.2 GaAlAsSb Materials Growth

Previous experiments on the liquid phase epitaxial growth of GaAlAsSb at 525°C and 500°C¹ share a fundamental limitation. The solubility of arsenic in the gallium melt is limited and consequently, only a small amount of arsenic can be incorporated in the solid. The result is shown in Fig. 4.2.

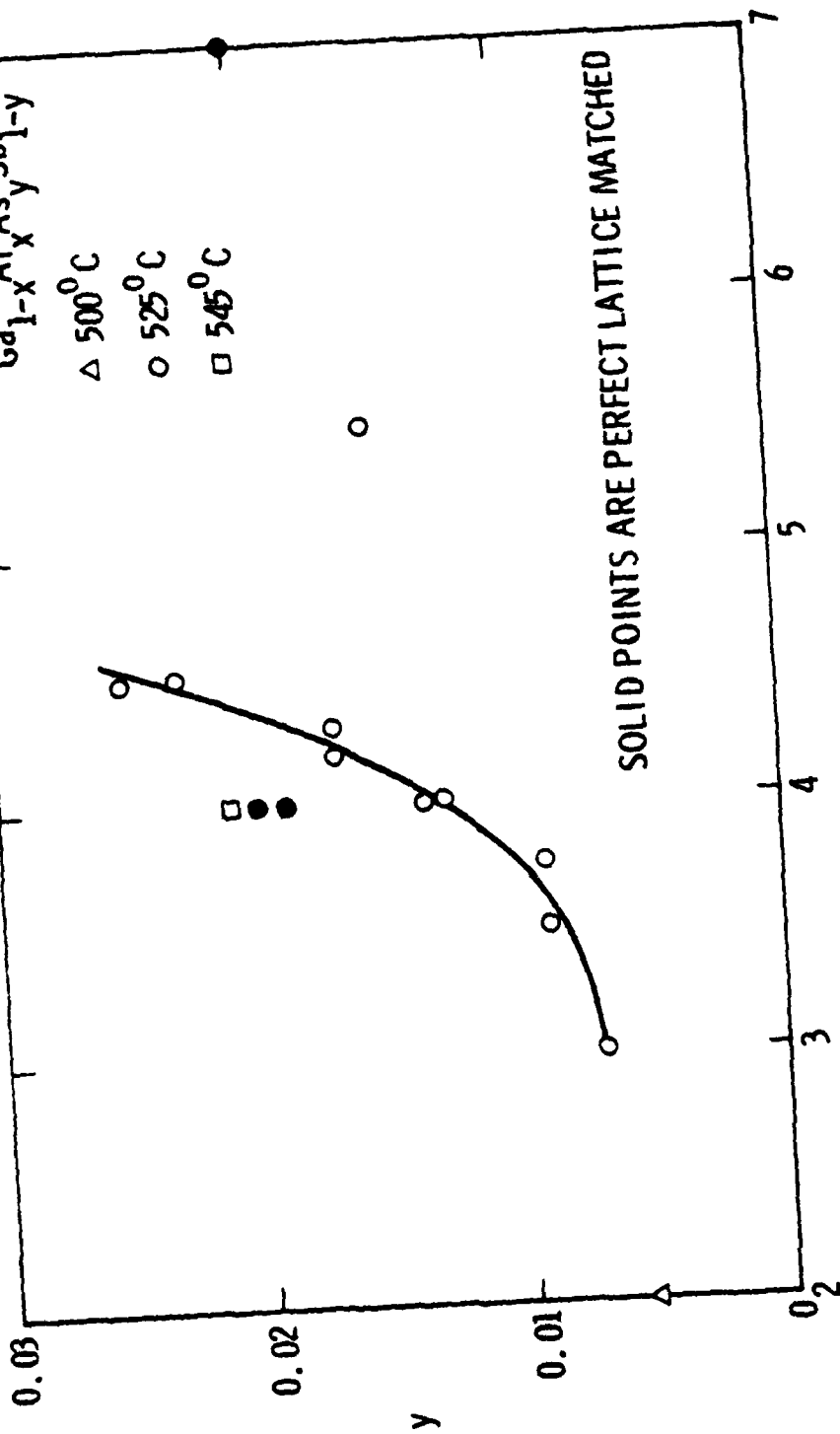
SC78-2231



Δ 500°C

\circ 525°C

\square 545°C



$10 \times X^I_{AS}$

Fig. 4.2 Arsenic liquidus in a gallium melt vs arsenic mole fraction in the solid.

Therefore, data were obtained for higher growth temperature, 550°C where the solubility of As in the Ga melt is increased. Epitaxial layers of higher quality were obtained.

For the growth of GaAlAsSb alloys at 550°C, the growth schedule followed G_1 , H_1 , J_1 , K_1 in Fig. 4.1. At H_1 the temperature of the furnace was equalibrated at $\approx 560^\circ\text{C}$ for at least half an hour and temperature ramping started at J_1 at a rate of $1/2^\circ\text{C}/\text{min}$. The epitaxial layers were grown at 2-3°C supersaturation. After the growth, the furnace was quenched down to room temperature.

Table 4.5 is a list of solubility data, saturation temperature (T_s), growth temperature (T_g), energy gap (λ_g) and lattice mismatch data ($\Delta a/a$), of several GaAlAsSb growth around 550°C. The melt compositions are given in mole fraction. The lattice mismatch was measured by a double crystal reflectometer using a $\langle 111 \rangle$ reflection from a high purity Si as the first reflection crystal. The $K\alpha_2$ was filtered by a slit. A Poisson's ratio of 0.29 has been assumed. The resolution for the set up can distinguish a 0.01% shift in lattice spacing. Figure 4.3 illustrates an x-ray rocking curve of a GaAlAsSb epitaxial layer lattice matched to within 0.012% to GaSb. The linewidth of the peak is greater than expected from theory. This broadening is probably due to the crystal quality. The best result, obtained on an undoped GaSb substrate, indicated a FWHM of approximately 50 seconds.

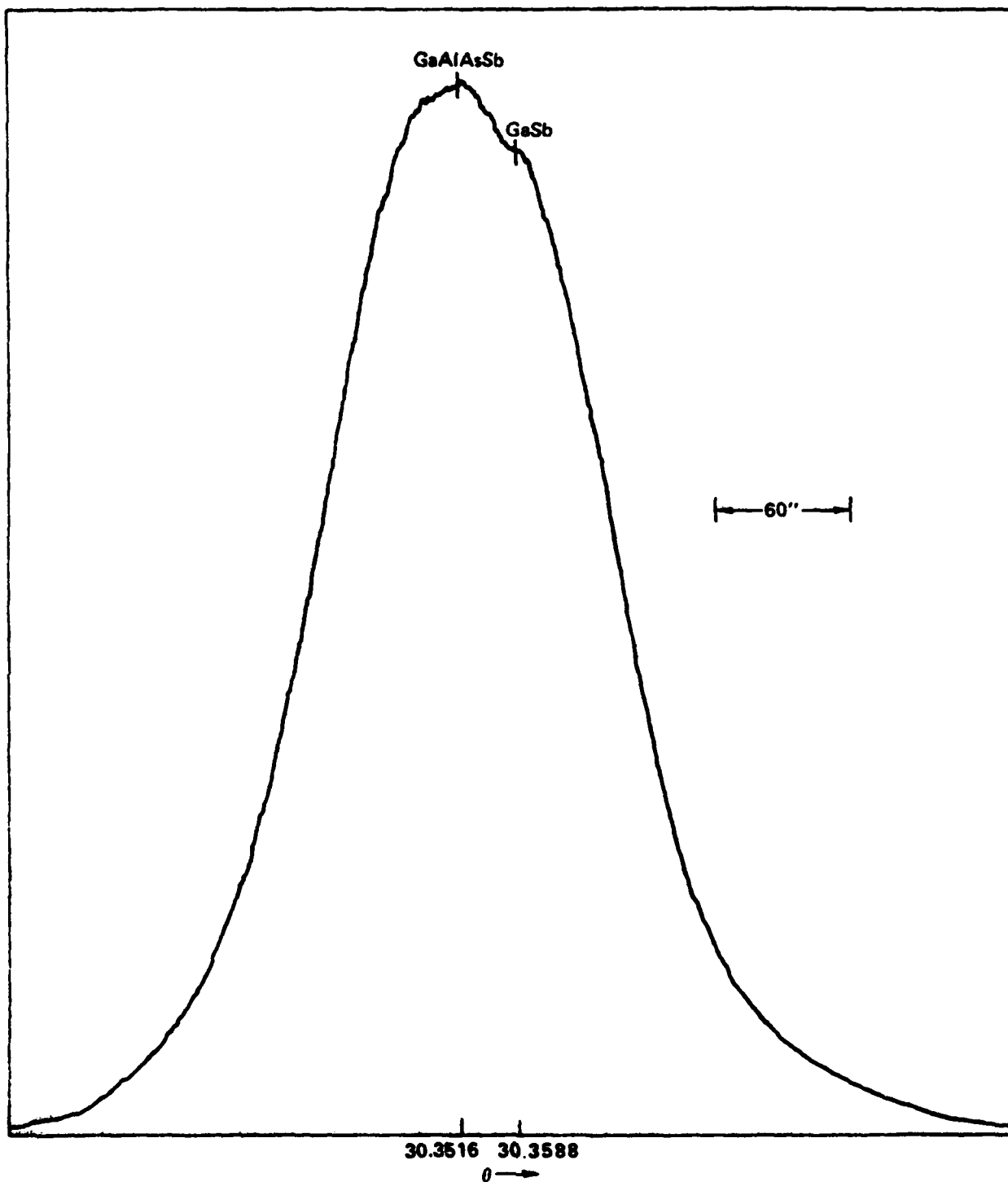


Fig. 4.3 X-ray rocking curve of a GaAlAsSb epitaxial layer lattice matched to within 0.012% to GaSb.

Table 4.5
Data for 550°C GaAlAsSb Growth

x_{Al}^I	x_{Sb}^I	x_{As}^I	T_s (°C)	T_g (°C)	λ_g (μm)	$\Delta a/a_0$ (%)
0.0278	0.031	6×10^{-4}	552	550	0.94	0.158
0.0278	0.031	7×10^{-4}	552	549	-	0.122
0.0278	0.031	8×10^{-4}	552	549	-	0.0953
0.0278	0.031	9×10^{-4}	552	549	-	0.0867
0.0278	0.031	-	551	549	-	0.339
0.025	0.0322	9×10^{-4}	550	547	0.96	-
0.0103	0.046	7×10^{-4}	548	545	1.23	<0.01
0.0103	0.046	6×10^{-4}	548	546	1.23	0.026
0.0103	0.046	5×10^{-4}	548	546	-	0.0433
0.0103	0.046	4×10^{-4}	548	546	-	0.0383
0.0103	0.046	3×10^{-4}	548	546	-	0.0594
0.0103	0.046	-	548	546	-	0.13
0.008	0.048	4×10^{-4}	550	547	1.30	0.012
0.007	0.049	3.5×10^{-4}	549	546	1.32	<0.03
0.006	0.052	3×10^{-4}	552	549	1.38	<0.03

There were two sets of lattice matching experiments done at 550°C. Figure 4.4 shows the lattice matching with various arsenic concentrations in a melt with the mole fractions of Al (x_{Al}^I) fixed at 0.0103 and x_{Sb}^I fixed at 0.046 (suitable for 1.27-1.3 μm detectors). With a x_{As}^I of 7×10^{-4} , the lattice mismatch is less than 0.01%. Without arsenic, the lattice mismatch is 0.13%. Figure 4.5 shows a similar experiment done on a higher aluminum content alloy. With x_{Al}^I fixed at 0.0278, x_{Sb}^I at 0.031 and x_{As}^I at 9×10^{-4} (suitable for APD window layers) the minimum lattice mismatch obtained is 0.0867%. Without any arsenic, the lattice mismatch of this alloy is 0.339%.

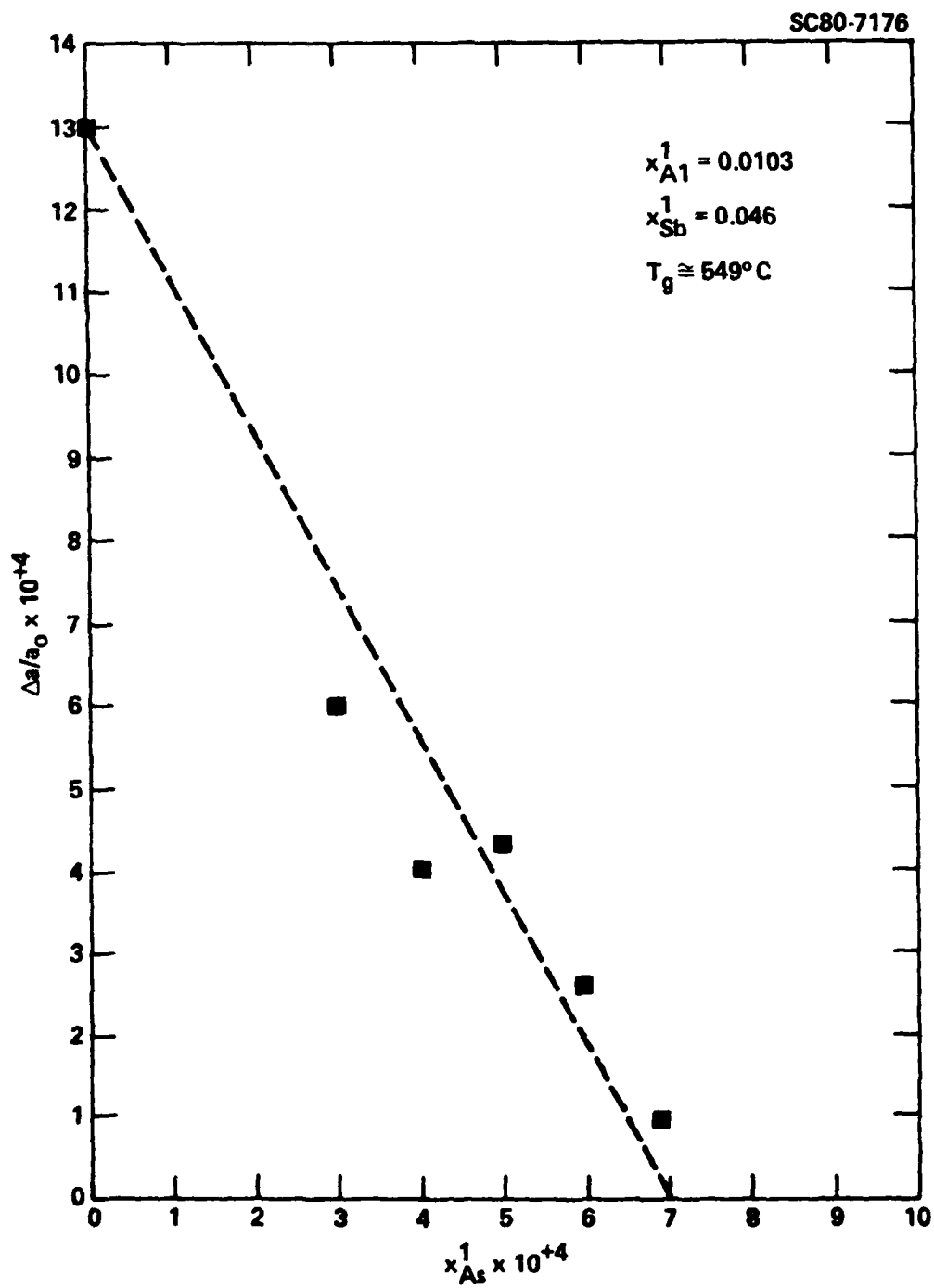


Fig. 4.4 Lattice mismatch as a function of arsenic in the liquidus (atomic fraction).

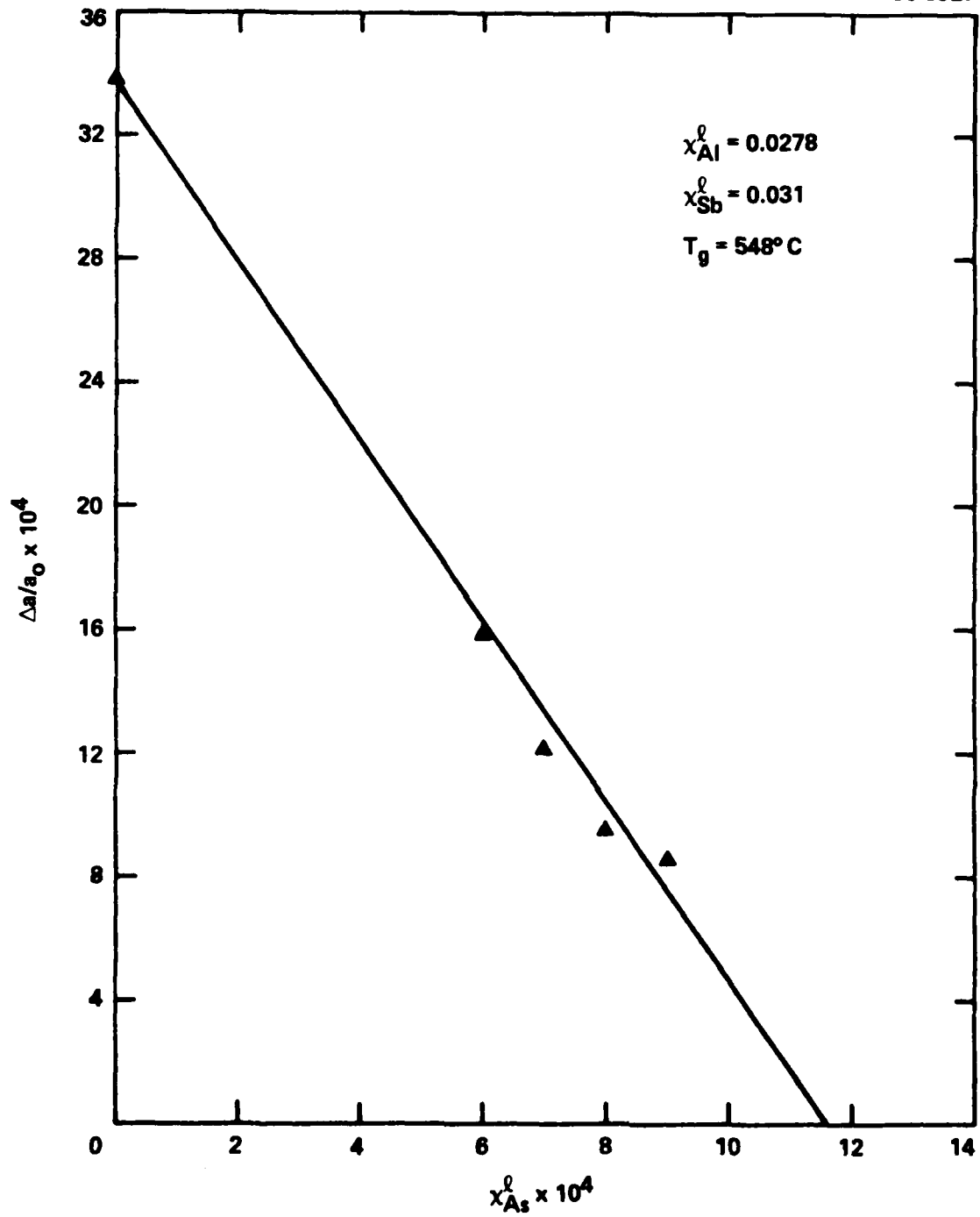


Fig. 4.5 Lattice mismatch as a function of arsenic in the liquidus at high Al content.

The saturation temperature increased by 50°C if more arsenic was added to the melt. This abrupt change caused growth on the high arsenic side of the phase diagram. The growth temperature was increased to 575°C and 590°C in an attempt to incorporate more arsenic in the alloy. However, device quality crystals were not obtained at these high temperatures. Evidently, if the growth temperature is increased to 620°C, good crystallization could be obtained again, since Motosugi and Kagawa² have reported high quality epitaxial GaAlAsSb crystals grown at 635°C. The distribution coefficient of arsenic at 550°C varies with Al composition in the two alloys as evident by comparing Figs. 4.4 and 4.5. This can be attributed to the growth rate of crystal as well as chemical kinetics. At a lower growth rate [higher aluminum content], the arsenic distribution is higher. Perturbations in the distribution coefficients are not uncommon. Feng et al³ has observed a perturbation in distribution coefficients in InGaAsP system when dopants were added.

One of the major problems in doping the GaAlAsSb alloys is that the amount of doping required in the melt changes with compositions of the alloys.⁴ Therefore, for each alloy composition, a separate doping calibration must be performed. Tellurium is commonly used to dope the epitaxial layer to n-type or low p-type concentrations, while germanium is used to dope the epitaxial layer to high p-type concentrations. To illustrate the dependence of the distribution coefficients of the dopant on the alloy composition, we obtained data on tellurium mole fractions required to dope the epitaxial layer to $1 \times 10^{16} \text{ cm}^{-3}$ on different alloy compositions. For 55%, 23% and 20% Al to

Ga ratio alloys, x_{Te}^1 of 1.82×10^{-8} , 6.19×10^{-8} and 6.55×10^{-8} are required to achieve $1 \times 10^{16} \text{ cm}^{-3}$ n-type epitaxial layers.

4.2 Heterostructure Avalanche Photodiode Development

The heterostructure APD's utilized in this program were grown by LPE on GaSb substrates utilizing melts composed as described above. The active region was one of two structures: (1) GaAlAsSb lattice matched to the GaSb substrate or (2) GaAlSb grown with one grading layer of GaAlSb. The lattice matched material gave higher performance devices and will be emphasized in this section.

After growth of the layers, ohmic contacts were deposited and alloyed. Si_3N_4 antireflection coatings were then applied to the top of the layer and mesas were patterned and etched to a depth sufficient to pass through the p-n junction. The devices were mounted on special high frequency packages for pulse measurements or tested in wafer form for low frequency measurements.

The dark current-voltage characteristics of a typical heterostructure GaAlAsSb avalanche photodiode is shown in Fig. 4.6. Notice the saturation characteristic of the reverse dark current. This diode has an active area of $2 \times 10^{-3} \text{ cm}^2$. Like most of the GaAlAsSb APDs, the initial dark current is quite high ($2 \times 10^{-6} \text{ A}$). However, the dark current is well-behaved until breakdown multiplying slower than the optical gain. This behavior suggests that a large surface leakage exists in these diodes. This is confirmed by the

MRDC81-11527

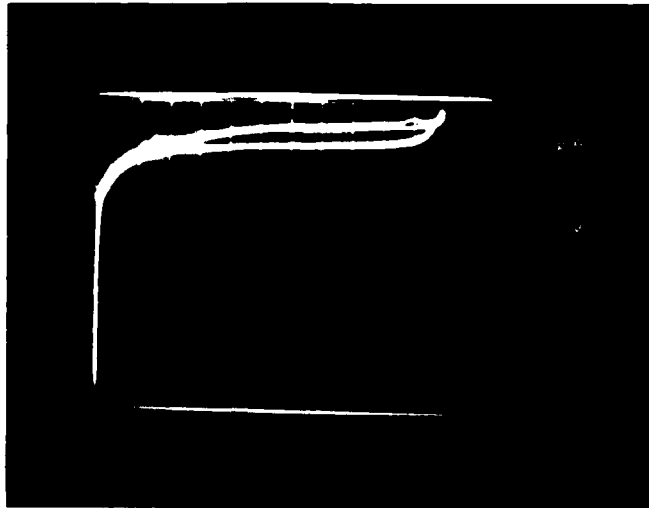


Fig. 4.6 Typical reverse characteristic of GaAlAsSb APD.

fact that with some mesa forming procedures photoresponse is seen far from the mesa, indicating the presence of surface inversion. The dark current at breakdown is approximately 8×10^{-6} A.

Figure 4.7 shows the capacitance-voltage relationship and doping profile of the same device. The doping is shown to be approximately 4×10^{15} cm^{-3} and is quite constant. The capacitance measurement showed a $1/C^2$ dependence indicating an abrupt junction existed. Thus the germanium used to dope the p^+ window layer did not diffuse into the active layer.

The photoresponse [normalized quantum efficiency] of a heterostructure APD is shown in Fig. 4.8. The diode did not have antireflection coating and was biased at 10 V. The abrupt cut-off at $1.3 \mu\text{m}$ results from the steep absorption edge of the active layer. The slower drop off at $0.96 \mu\text{m}$ was due to the indirect bandgap window layer. The quantum efficiency is quite flat from $1.0 \mu\text{m}$ to $1.3 \mu\text{m}$ and is approximately 67%. The residual tail of the photoreponse at shorter wavelength is due to the absorption on the surface of the window layer which is approximately $2 \mu\text{m}$ thick. Quantum efficiency as high as 96% was observed in the heterojunction GaAlAsSb APD with antireflection coatings at $1.06 \mu\text{m}$. Normally, the quantum efficiency with antireflection coating is higher than 88%.

The speed of the heterostructure diode is faster than most systems requirements. To illustrate the speed capability of these devices, smaller area diodes were mounted in a high speed package and a Nd-YAG mode-locked laser was used to test the response of the diode. The diode was connected directly

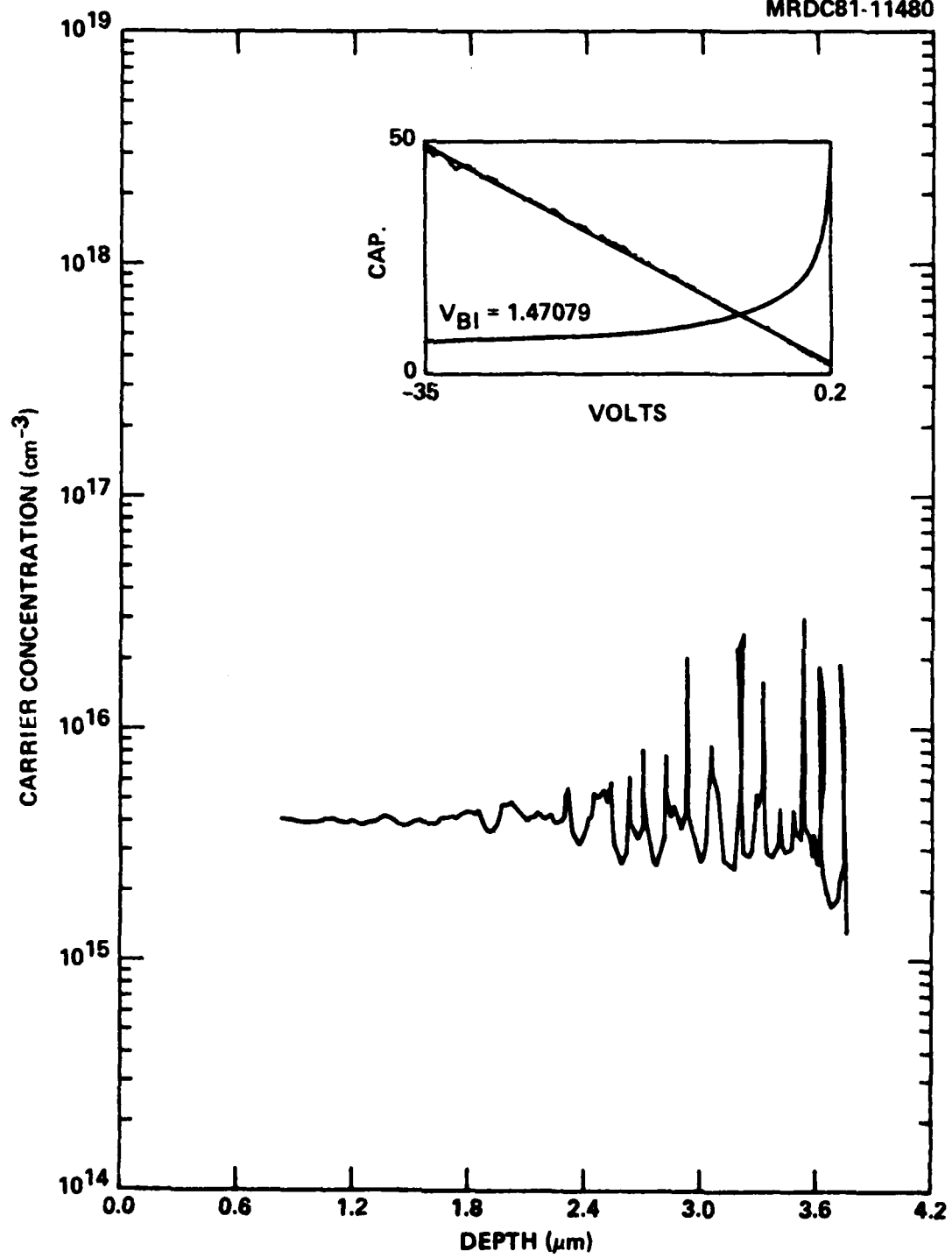


Fig. 4.7 Capacitance-voltage and doping profile of a GaAlAsSb heterojunction APD.

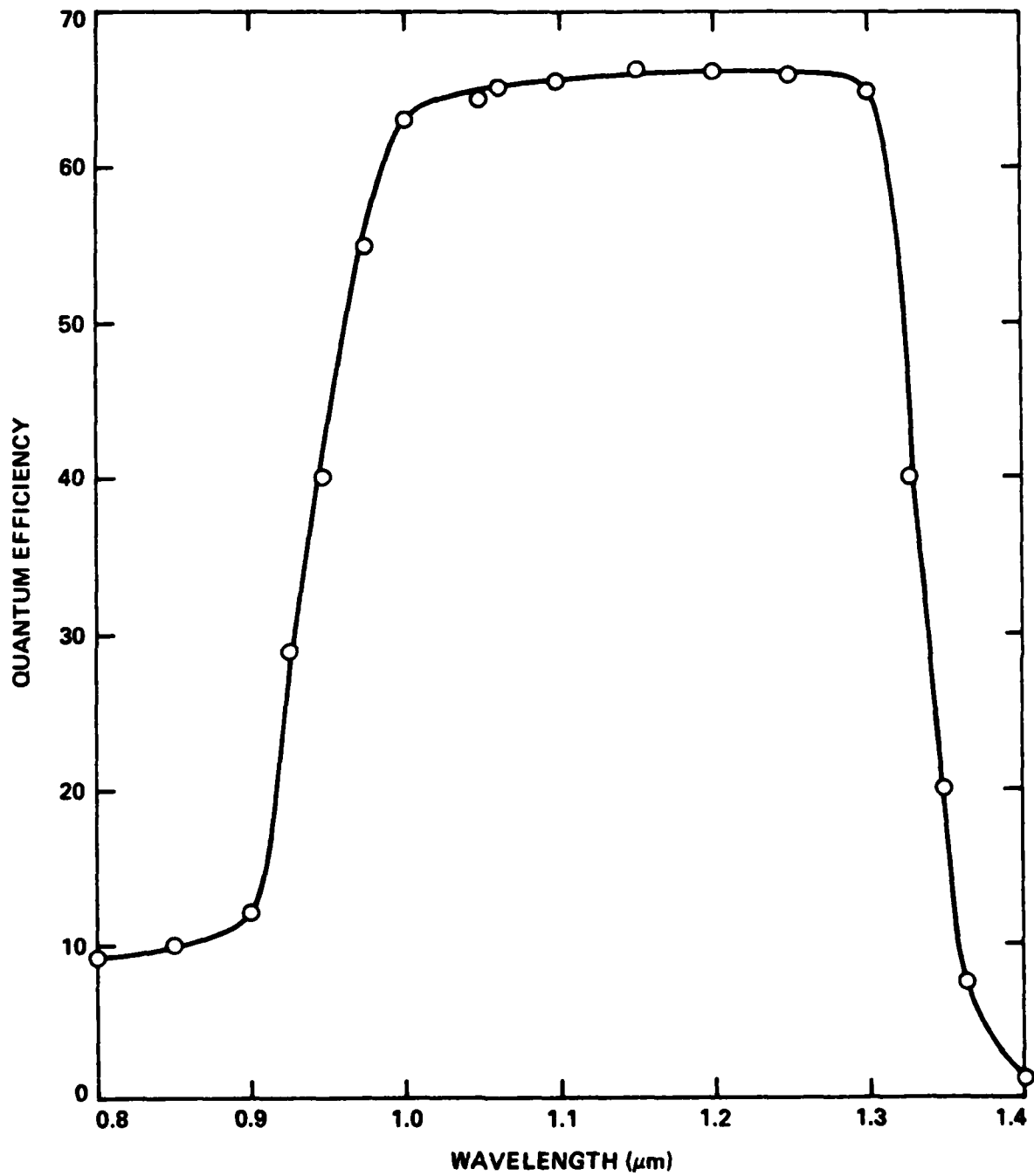


Fig. 4.8 Photoresponse of a GaAlAsSb heterojunction APD.

to a Tektronics S-4 sampling head. Figure 4.9 shows the response with 60 psec risetime and 120 psec FWTM. To illustrate the importance of the heterojunction design with respect to the high speed application, Fig. 4.10 shows the response from the same diode under different illumination conditions. The top picture shows the 1.06 μm mode-locked laser response in which the absorption is in the depletion region. The bottom picture shows the 0.53 μm mode-locked laser response in which the absorption is on the surface of the window layer. The slow diffusion tail is caused by the carriers diffusion through the 2 μm window layer.

The uniformity of gain of the APD is extremely important to system application. Figure 4.11 shows a typical cross-section scan of a heterojunction APD. The lower trace was taken at unity gain. The upper trace was taken at a gain of 7 showing a fairly uniform gain. Figure 4.12 shows the intensity modulation scan of an GaAlAsSb APD. The photoresponse of the diode was intensity modulated and displayed on a scope. The bright area shows a high response. This picture was taken at a gain of 21. A very uniform gain was observed. [Any nonuniformity of the electric field inside the diode will be amplified by almost two orders of magnitude by gain].⁵

The best microwave gain observed in any heterojunction GaAlAsSb APD is shown in Fig. 4.13. A mode-locked Nd-YAG laser having a repetition rate of 273 MHz was used to excite the diode. The diode was connected to a B&H 3002 amplifier and a Tektronix 7L13 spectrum analyzer. The spectrum analyzer was tuned to pick up the 273 MHz signal and the output was monitored on the y-axis of the x-plot while the bias voltage of the diode was measured on the

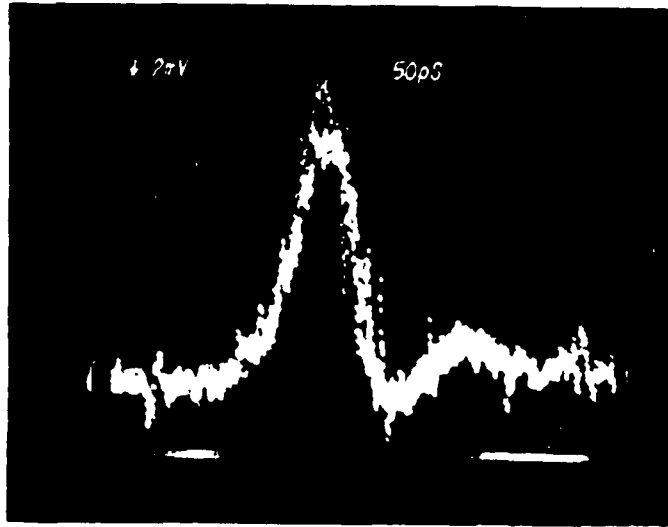


Fig. 4.9 Photograph of the speed of response of a GaAlAsSb heterojunction APD.

MRDC79-3501

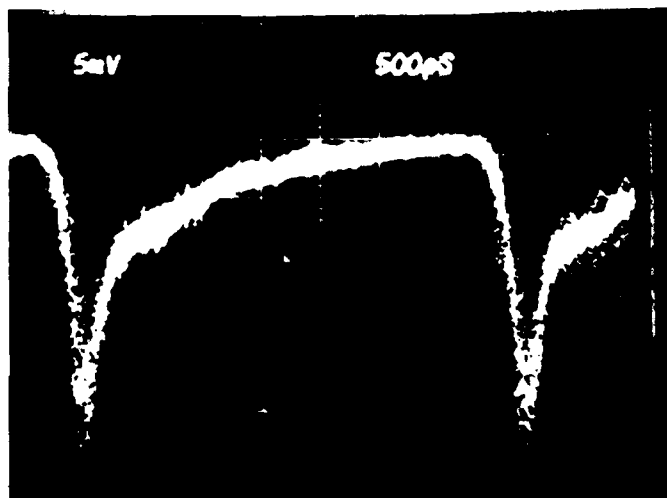
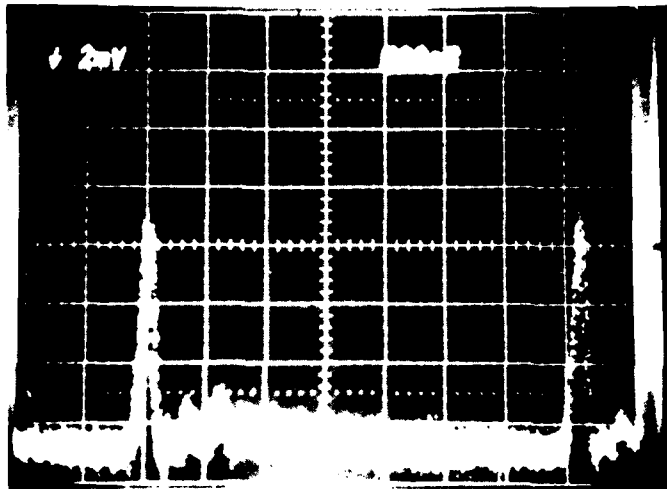


Fig. 4.10 The speed of response of a GaAlAsSb APD with absorption occurring (a) in the active layer; (b) in the window layer.

MRDC81-11528

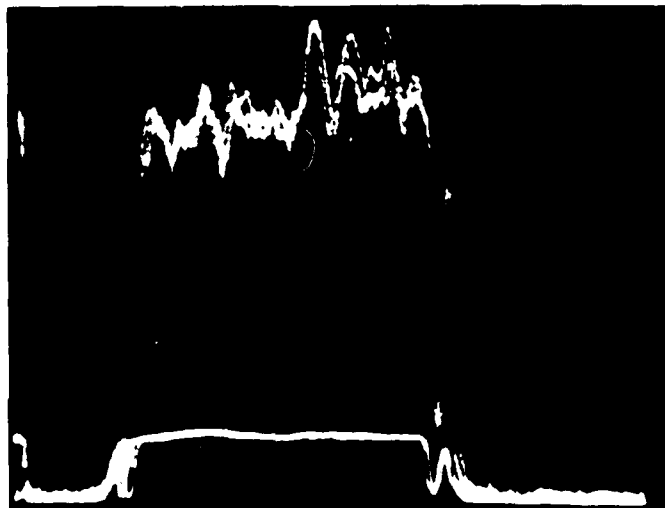


Fig. 4.11 Photograph of the uniform gain possible with a GaAlAsSb APD.

MRDC81-11466



Fig. 4.12 Photoresponse intensity modulated scan of a GaAlAsSb heterojunction APD.

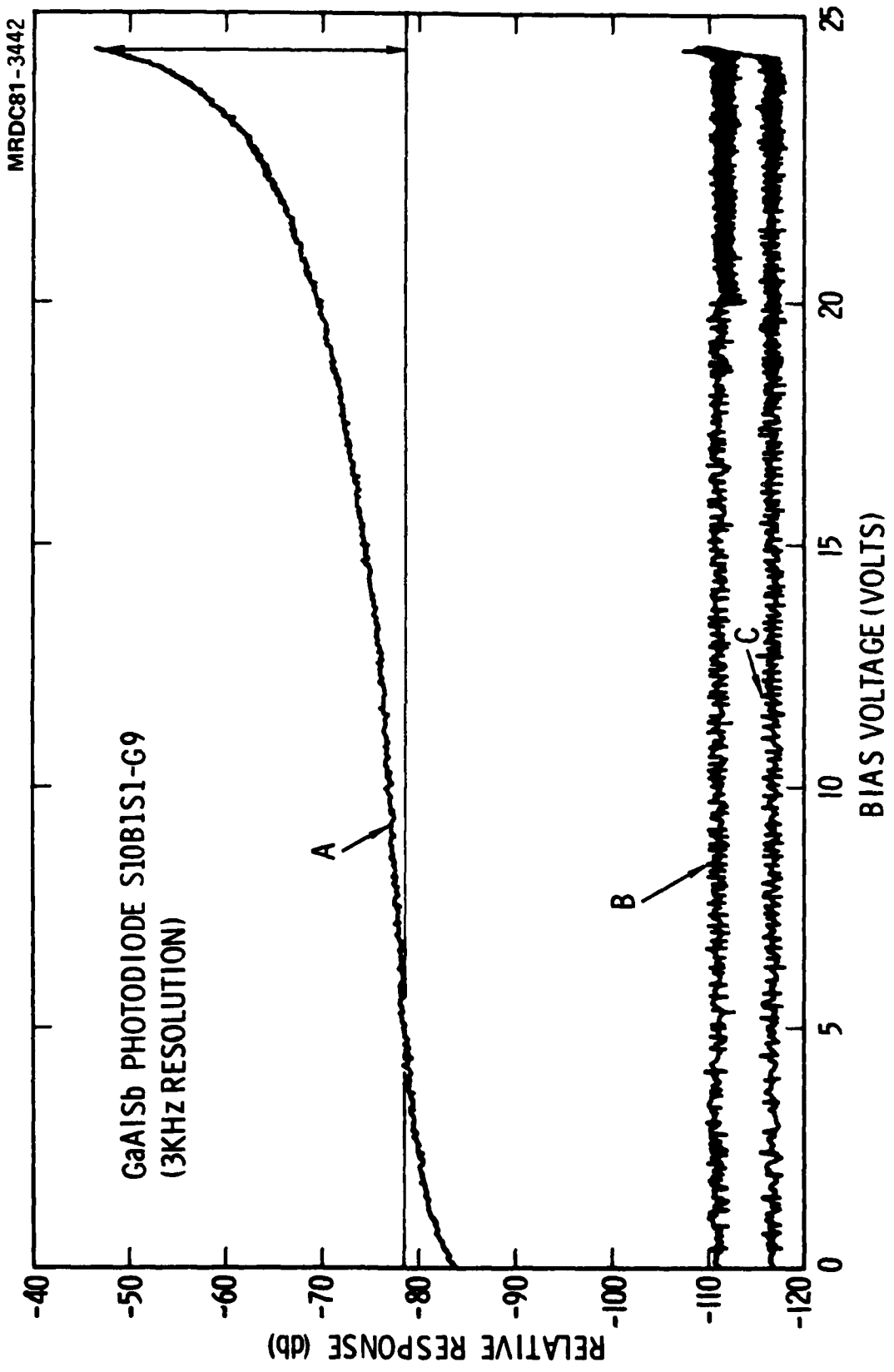


Fig. 4.13 Plot of microwave gain vs voltage of the best Be-implanted GaAs APD.

x-axis. Curve A shows a microwave optical current gain of 40. Curve B shows the corresponding dark noise of the measurement tuned at 273 MHz while curve C shows the detuned noise. Notice the breakpoint of the noise measurement (curve B) which happens to be almost the same bias as the gain of 40 on curve A. Therefore, the usable gain of the diode with this particular preamplifier is 40. This will confirm that most of the dark current in the GaAlAsSb APD is surface leakage which does not multiply and ruin the signal to noise ratio. Recall that the noise term $\langle i_n \rangle^2$ is:

$$\langle i_n \rangle^2 = 2qBI_s + 2qB(I_B + I_{ph})M^2F(M) + \text{amplifier noise}$$

where, B is the bandwidth; I_s , the surface leakage; I_B , the bulk leakage; I_{ph} , the photocurrent; M, the gain of the diode and F, the excess noise factor which is a function of M. If the bulk leakage current was the dominating factor and was in the 10^{-6} A range, the noise would be dominated by the excess avalanche noise long before the diode reached a gain of 40.

The existing problems in the heterostructure GaAlAsSb avalanche photodiodes are high surface leakage current and low yield. Consistently, we observed very high leakage current at low bias voltage and the leakage stayed at almost the same level until breakdown occurred. In several cases, we actually saw a flat reverse current as shown in Fig. 4.14. Although the surface current does not multiply with gain and gives a high excess avalanche noise at high gain, it will ultimately lower the sensitivity of the diode. The yield of high performance [uniform high gain; reasonable dark current]

MRDC80-11019

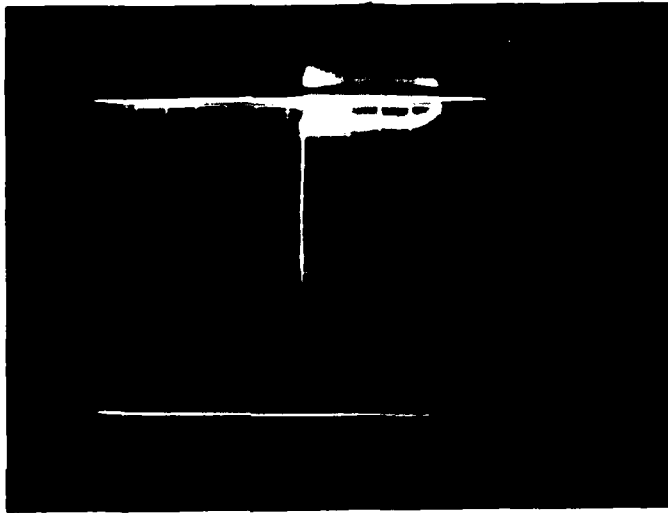


Fig. 4.14 Reverse I-V characteristic demonstrating the effect of high surface leakage.

GaAlAsSb avalanche photodiodes is low at present. The improvement of yield will rely on the crystal development.

4.3 Ion Implanted GaAlAsSb Avalanche Photodiode

The success in fabricating InGaAsP avalanche photodiodes by ion implantation led to the development of ion implanted GaAlAsSb avalanche photodiode.

We found that both the dosage and energy of the Be-implanted structure are very important to the quantum efficiency of the photodiode. For example, in the homojunction structure of the GaAlAsSb diode, with an implant dosage of $5 \times 10^{14} \text{ cm}^{-2}$ and implant energy of 100 keV on bare surface, we obtained less than 20% quantum efficiency in the avalanche photodiodes. Subsequently, we reduced the dosage to 5×10^{13} and energy to 80 keV, the quantum efficiency went up to 48%. Recently, we used a $1 \times 10^{13} \text{ cm}^{-2}$ dosage of Be at 70 keV, and the Be was implanted through 1650 Å of Si_3N_4 , and we obtained a tremendous increase of quantum efficiency. In several cases, 90% quantum efficiencies have been obtained. This high quantum efficiency is due to a much shallower junction. The short distance that the carriers have to diffuse or even a surface field will cause the electrons to drift through the junction before they have a chance to recombine. A list of estimated junction depths versus implant dosages and energies is shown in Table 4.6.

Table 4.6
 Estimated Junction Depths of Different Implant
 Energy and Dosage of Be; After 450°C, 10 min
 Annealing; the Background is Assumed to be
 $1 \times 10^{16} \text{ cm}^{-3}$

Energy	Dosage	Junction Depth
100 keV	$5 \times 10^{14} \text{ cm}^{-2}$	1.2 μm
100 keV	$1 \times 10^{14} \text{ cm}^{-2}$	1.0 μm
80 keV	$1 \times 10^{14} \text{ cm}^{-2}$	0.7 μm
80 keV	$5 \times 10^{13} \text{ cm}^{-2}$	0.5 μm
70 keV	$5 \times 10^{13} \text{ cm}^{-2}$	0.3 μm
70 keV	$1 \times 10^{13} \text{ cm}^{-2}$	0.2 μm

Low energy beryllium ions were used to form p-n junctions in GaAlAsSb layers. The layer was then annealed at 450°C for 30 minutes to activate the ions. It was then processed into mesa diodes the same way as the heterostructure APD. Since the p-n junction is a homojunction a better gain uniformity and dark current are expected.

A typical spectral response of an ion implanted $\text{Ga}_{0.8}\text{Al}_{0.2}\text{As}_x\text{Sb}_{(1-x)}$ diode is shown in Fig. 4.15. The diode did not have an antireflection coating. The peak response is at 1.29 μm with an external quantum efficiency of approximately 56%. The response falls off slightly at shorter wavelengths due to surface recombination.

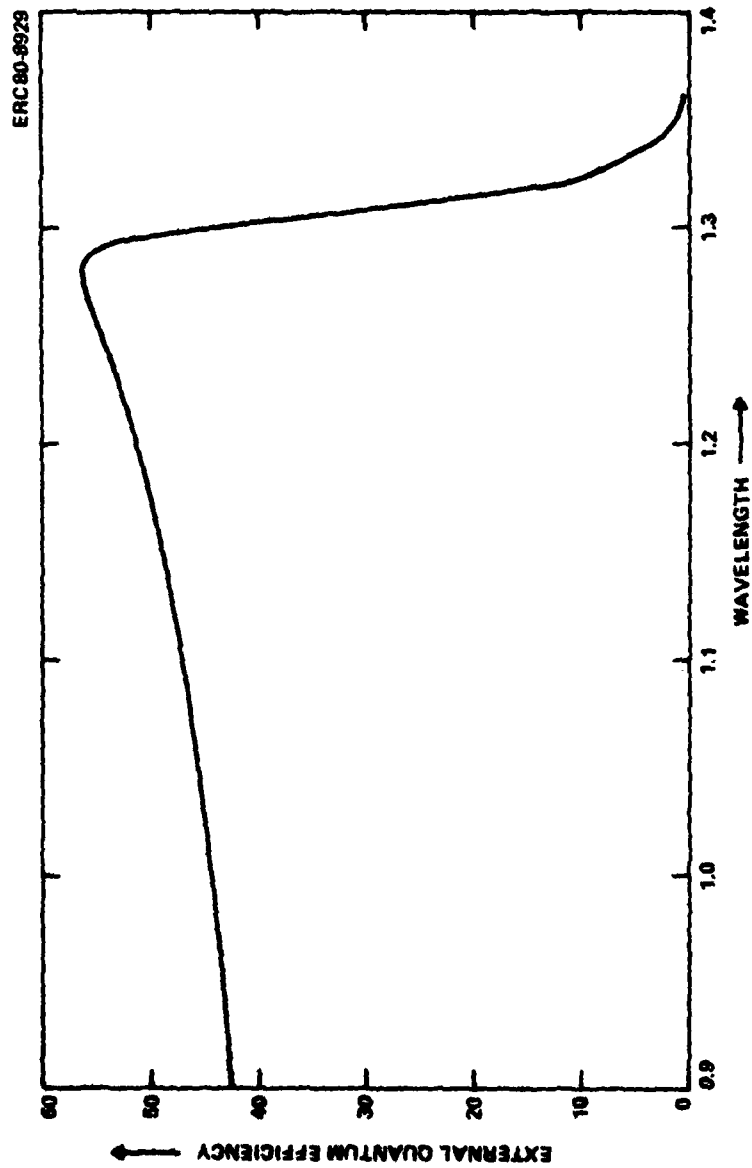


Fig. 4.15 External quantum efficiency vs wavelength of a Be-implanted GaAlAsSb avalanche photodiode without antireflection coating.

The speed of the ion implanted homojunction GaAlAsSb diode is not as fast as the heterojunction diodes. Small diodes (5 mil diameter) exhibit 400 psec FWTM.

Figure 4.16 shows the I-V characteristics of an ion implanted diode. At half of the breakdown voltage, the leakage is approximately 20 μ A which is comparable to the heterostructure diodes.

The homojunction GaAlAsSb APDs provide very high gain at a test wavelength 1.06 μ m. Figure 4.17 shows a 273 MHz gain of such an avalanche photodiode. The microwave optical gain is 41 dB. The bottom curve shows the corresponding noise measurement. The breakpoint occurs at the bias voltage having the 41 dB gain. The 41 dB gain was not the highest gain, but at higher gain the excess noise dominates.

The uniformity of gain in an ion implanted GaAlAsSb diode is excellent. Figure 4.18 shows an intensity modulated photoresponse of a diode biased at a gain of 90. There is a slight gain depression on the right bottom half of the diode. However, the uniformity is better than $\pm 5\%$ over the whole area.

4.4 Hole Injection Avalanche Photodiode

To implant the hole injection structure shown in Fig. 4.4, several layers of $\text{Ga}_{0.55}\text{Al}_{0.45}\text{As}_x\text{Sb}_{(1-x)}$ were grown at 550°C to calibrate the doping. The lowest we obtained was approximately $8 \times 10^{16} \text{ cm}^{-3}$ which is not low enough for the hole injection structure. Also, calibration of the low

MRDC80-11018

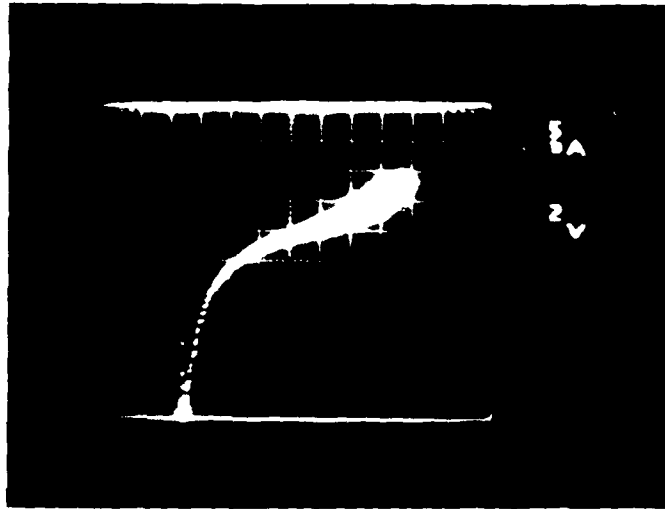


Fig. 4.16 Reverse I-V characteristic of a Be-implanted GaAsAsSb homojunction APD.

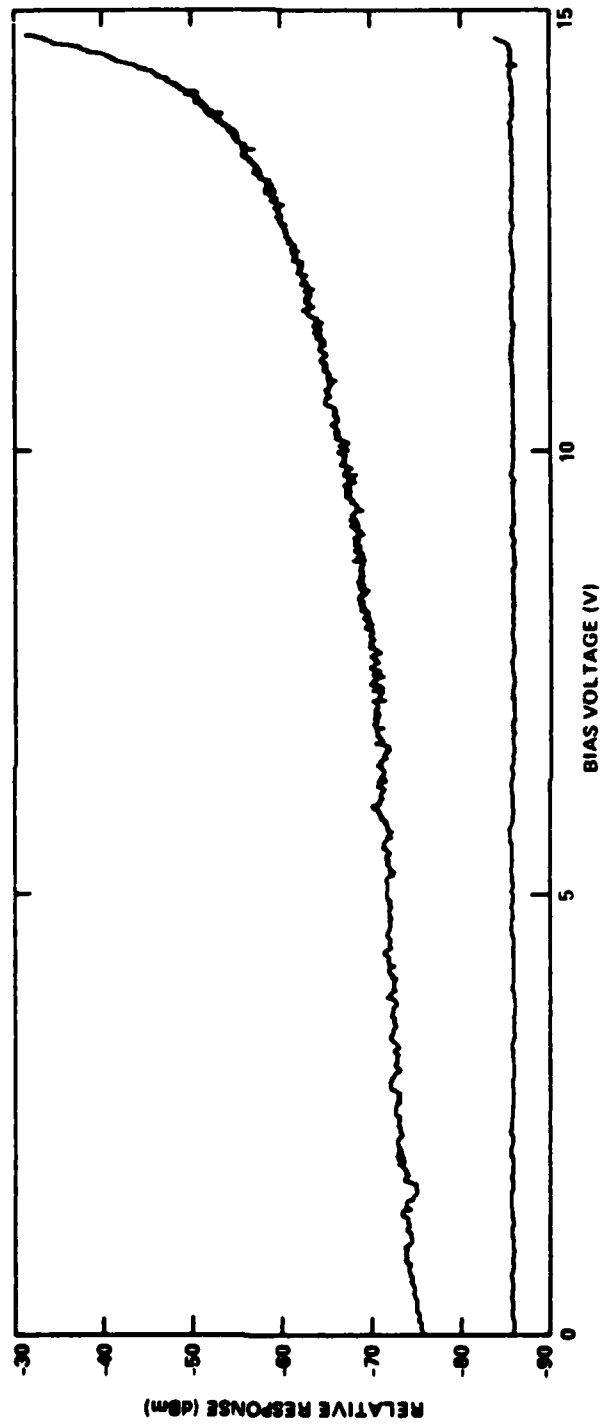


Fig. 4.17 Gain vs bias voltage of a Be-implanted GaAlAsSb homojunction APD.

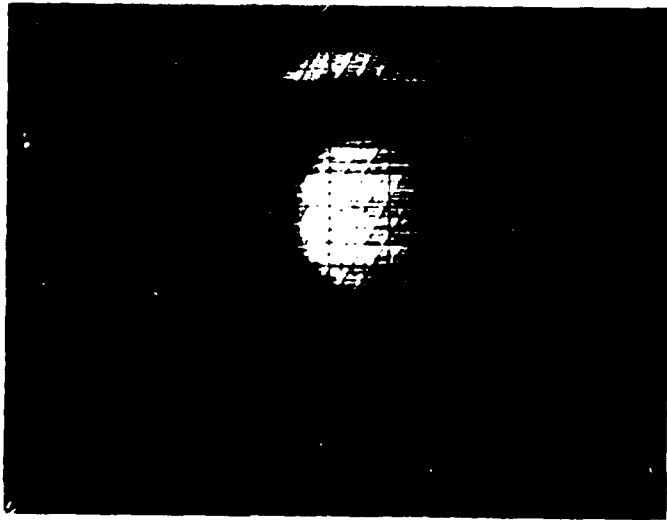


Fig. 4.18 Intensity modulated scan of an ion implanted GaAlAsSb APD at 273 Mhz and gain of 90; showing uniformity of gain over entire optical area to 10% .

temperature $\text{Ga}_{0.55}\text{Al}_{0.45}\text{Sb}$ was done. Although the growth parameters were never quite optimized for this structure, we succeeded in fabricating some avalanche photodiodes. For these diodes, the window layer was too thick, and the field did not punch through at breakdown.

Figure 4.19 shows the photoresponse of the diode. The response is highest at wavelengths shorter than $0.95 \mu\text{m}$ which is the bandgap of the window layer, indicating the absorption at the surface. From $0.95 \mu\text{m}$ to $1.32 \mu\text{m}$, the response is moderate. This region reflects the absorption of photons in the absorbing layer which has a bandgap of 0.94 eV . Beyond $1.32 \mu\text{m}$, there is very little response indicating the absorption is in the GaSb substrate. These diodes have quantum efficiency of less than 10% at $1.27 \mu\text{m}$ and is the result of the non-punch-through structure. If the punch-through occurs, the region between $0.95 \mu\text{m}$ and $1.32 \mu\text{m}$ will be the highest, and the quantum efficiency will be expected to be higher than 85%. Nevertheless, we observed a gain higher than 30 in this diode. Figure 4.20 illustrates the gain vs reverse bias voltage. The sloping baseline at low bias caused by the depletion region widening effect.

4.5 Schottky Barrier Avalanche Photodiodes

Schottky barrier avalanche photodiodes have also been fabricated in the $\text{Ga}_{1-x}\text{Al}_x\text{As}_{1-y}\text{Sb}_y$ ($y > 0.97$) alloy system. Although these devices are not expected to have high performance, they serve as a material study tool. The devices are planar and have semi-transparent Au-barriers. These detectors

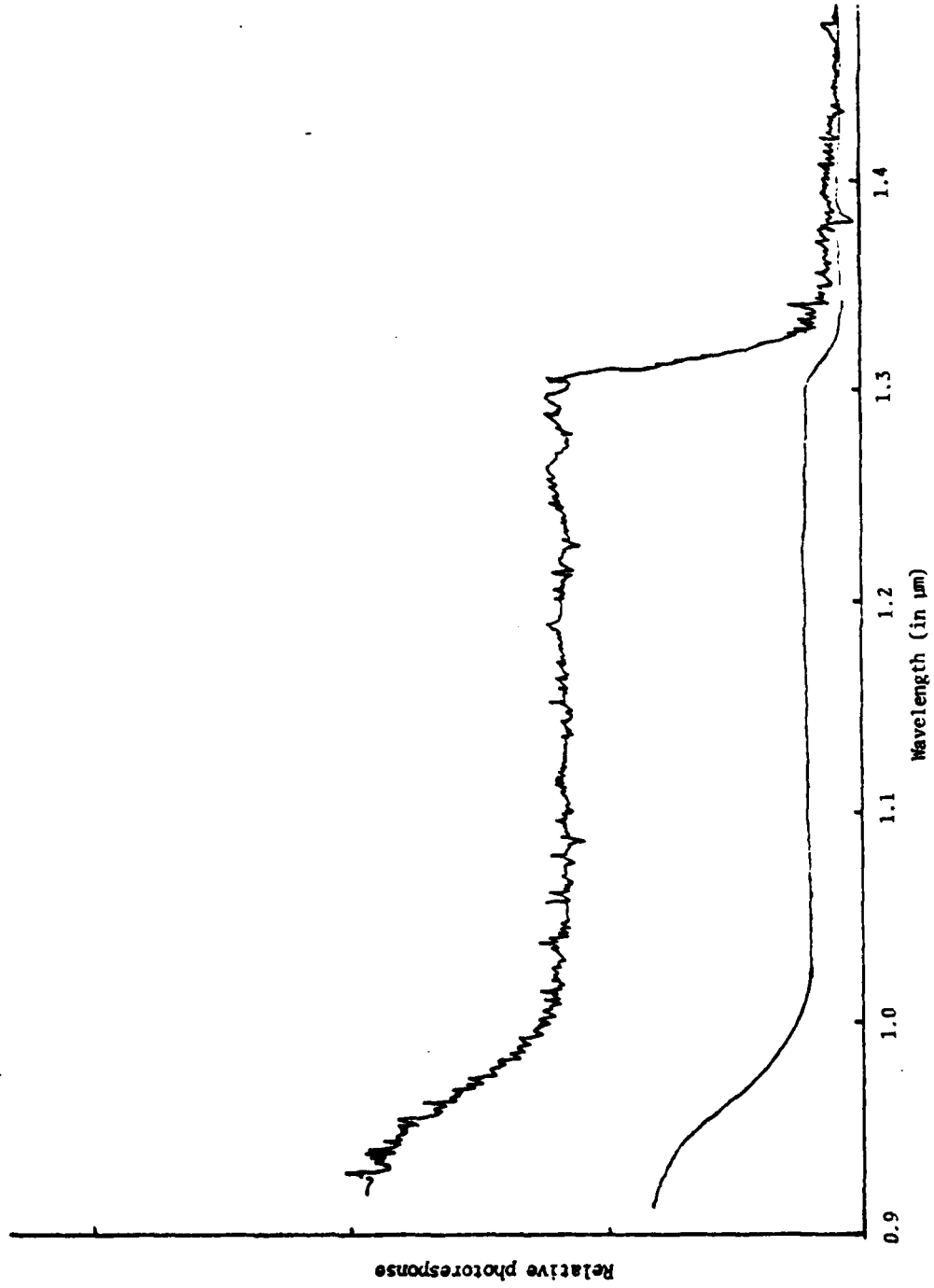


Fig. 4.19 Photoresponse of the hole injection GaAlAsSb photodiode with too thick a window layer..

461510

Fig. 4.20 Gain vs voltage of a hole injection GaAlAsSb photodiode.

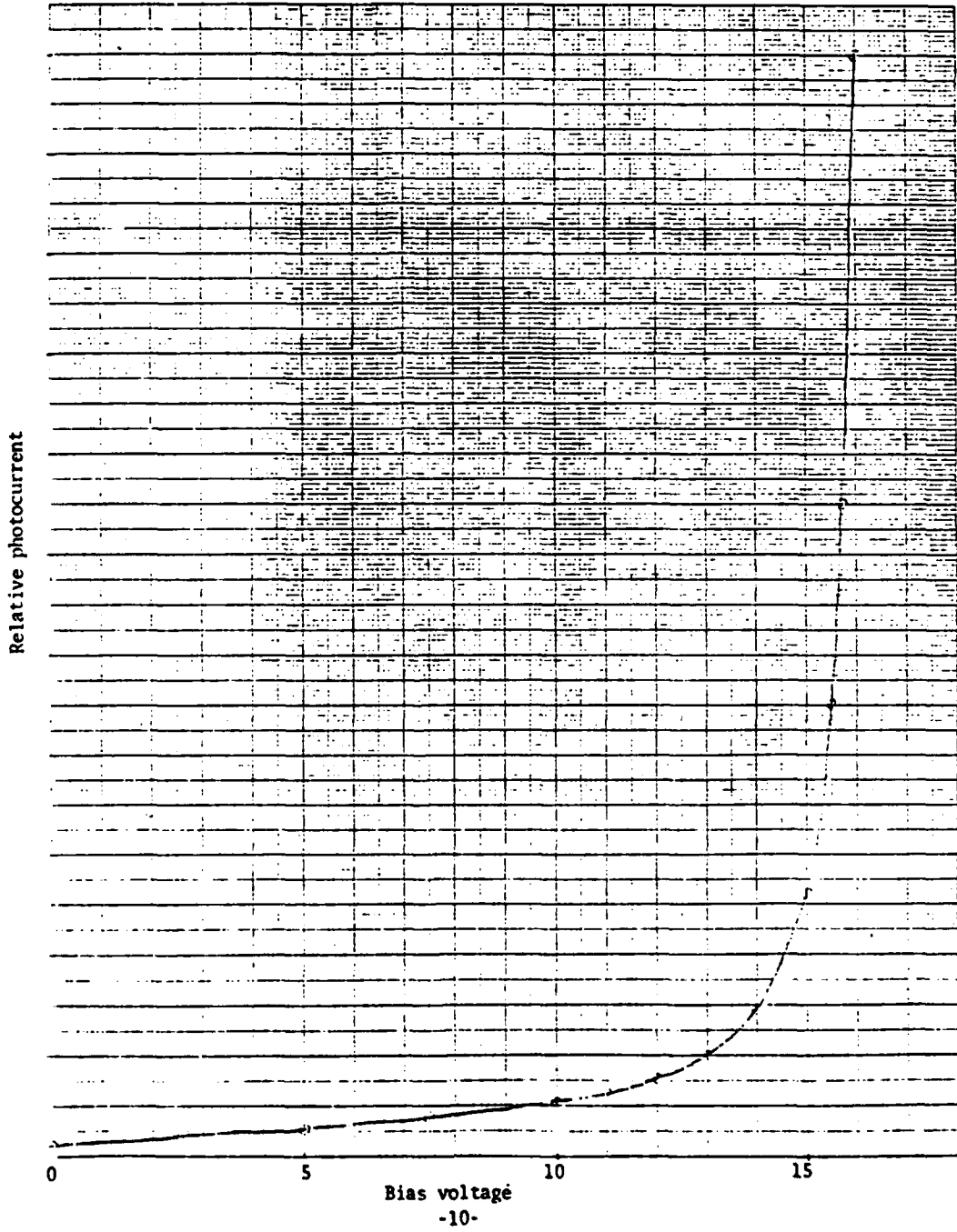
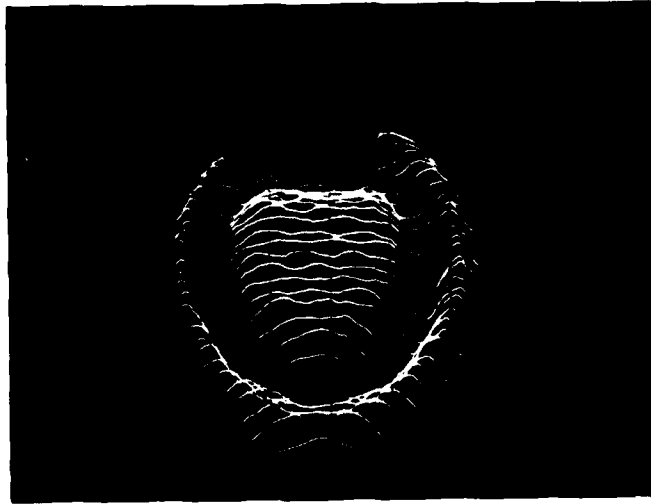


Fig. 4.20 Gain vs voltage of a hole injection GaAlAsSb photodiode.

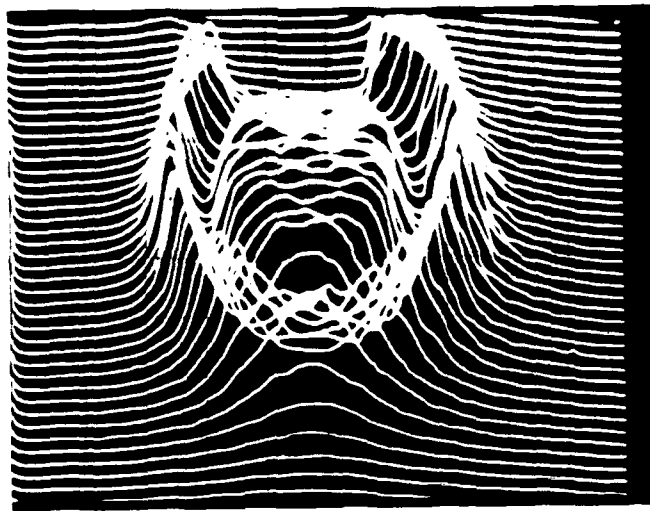
exhibit uniform photoresponse; and dark current densities of $\sim 2.7 \times 10^{-3}$ A/cm² at avalanche gains of 2 to 4 have been measured. Photon absorption occurs in the 4 μ m thick Ga_{1-x}Al_xAs_{1-y}Sb_y epitaxial layer. This layer is doped with Te to a net bulk carrier concentration $N_D - N_A \sim 2 \times 10^{16}$ cm⁻³. N-type GaSb serves as the substrate. As in the other configurations, the absorption can be varied by adjusting the Al concentration in the epilayer.

The dark current and photoresponse of the devices were measured in wafer form on a probe stage. Dark current densities of $\sim 2.7 \times 10^{-3}$ A/cm² at an avalanche gain of 2-4 have been obtained. The abruptness of the reverse breakdown indicates that it is dominated by edge effects. The uniformity of the diode photoresponse was examined by scanning the device with a focused Nd:YAG laser emitting at 1.06 μ m. Two photographs of the response profile of an Au-Ga_{1-x}Al_xAs_{1-y}Sb_y Schottky barrier photodiode obtained in this manner are shown in Fig. 4.21. In the upper photograph (a) the device is at zero bias and in the lower photograph (b) 20 V reverse bias. For all bias voltages $V < V_{br}$; the photoresponse is extremely uniform. This demonstrates the material is relatively free of defects and that breakdown is not controlled by the formation of microplasmas up to a gain of 4. As is evident from Fig. 4.21b the multiplication is higher at the edges than the rest of the device, as expected. The DC gain, defined as the ratio of photoresponse at approximately breakdown (V_{br}) and that at $1/2 V_{br}$ was obtained by chopping the incident light and recording the photoresponse from) V to 12 V reverse bias is small. With further structural changes, it should be possible to increase the multiplication factor and reduce the dark current further.

ERC80-8811



(a)



(b)

Fig. 4.21 Photoresponse profile of a Schottky barrier at
(a) zero bias; (b) 20 V reverse bias.

4.6 GaAlAsSb APD Leakage Study

The leakage current in the GaAlAsSb, GaAlSb p-n junctions is dominated by a surface leakage current. In some instances, we observed surface inversion. To elucidate this, Fig. 4.22 shows a raster scan of a thin Schottky barrier GaAlAsSb diode. There was a photoresponse within the Schottky barrier as expected. However, the response extended to several mils away from the active area. The diffusion length of this material is on the order of microns. Therefore, the response away from the active area was not due to carrier diffusion. Only an inverted surface will behave like this. Nevertheless, we only observed this problem in several instances, and the effect was sensitive to the processing technique.

We did several experiments with wet chemistry surface treatment. The leakage current of the p-n junction was monitored *before and after* the treatment. The results are summarized in Table 4.7.

In addition to the wet chemistry treatment we deposited different kinds of dielectrics on the surface of GaAlAsSb diodes. The results are summarized in Table 4.8. The thin aluminum evaporation before anodization is the most promising at present.



Fig. 4.22 Raster scan of a Schottky barrier GaAlAsSb diode with an inverted surface.

Table 4.7
Surface Treatments on GaAlAsSb

Solution	Time	Rinse	Comment
1 NH ₄ OH:1 H ₂ O	15 sec	H ₂ O-CH ₃ OH	No change
1 NH ₄ OH:1 H ₂ O	5 min	H ₂ O-CH ₃ OH	No change
1 NH ₄ OH:9 H ₂ O	1 min	H ₂ O-CH ₃ OH	No change
3 H ₂ O:4 NH ₄ OH:3 H ₂ O ₂	15 sec	H ₂ O-CH ₃ OH	Degrade
10 ml H ₂ O ₂ + 2 drops of NH ₄ OH	30 sec	H ₂ O-CH ₃ OH	Degrade
H ₂ SO ₄	45 sec	H ₂ O-CH ₃ OH	Slightly degrade
1 H ₂ SO ₄ :9 H ₂ O	30 sec	H ₂ O-CH ₃ OH	Slightly degrade
1 HF:9 H ₂ O 1 min		CH ₃ OH	Degrade
1 CH ₃ COOH:H ₂ O	30 sec	H ₂ O-CH ₃ OH	Slightly improve
Boiling H ₂ O 15 sec		H ₂ O	Slightly degrade
1 H ₃ PO ₄ :9 H ₂ O	15 sec	H ₂ O-CH ₃ OH	Degrade
Microstrip 15 sec		H ₂ O-CH ₃ OH	No change
0.5% Br-CH ₂ OH	15 sec	CH ₃ OH	Improve
1 KOH:1 K ₃ Fe(CN) ₆ 10H ₂ O	15 sec	H ₂ O-CH ₃ OH	Improve
16 Lactic Acid:1HNO ₃ :HF	15 sec	H ₂ O-CH ₃ OH	Improve

Table 4.8
Dielectric Coatings on GaAlAsSb

Method	Comment
Sputtered Si ₃ N ₄	Slightly improve
Plasma Si ₃ N ₄	Degrade
CVD SiO ₂	No change
Anodic Oxide	No change
Evaporate 100 Å Al and Anodized	Improve

The dominant noise term when the photodiode is operating at high gain is the excess noise. The bulk leakage current will multiply faster than the signal and degrade the signal to noise ratio. It is necessary, therefore, to minimize the bulk leakage.

To determine the generation centers in GaAlAsSb diodes, we did a temperature study of the current-voltage relationship of the diode. Figure 4.23 shows a forward characteristic of a GaAlAsSb diode vs temperature. At any measured temperature the ideality factors, n , were higher than two, indicating surface current existed. Figure 4.24 shows the reverse characteristics of the same diode. At high temperature close to room temperature, the leakage current was only slightly dependent on the bias voltage. At lower temperatures, clearly shown were two components of the leakage. The steep region was thought to be tunneling current. To find out the activation energy of the generation centers, we plotted $I/T^{5/2}$ vs I/T on a semilog plot.⁶ The slope corresponded to an activation energy of 0.216 eV. If these generation centers can be eliminated in the crystals, the bulk leakage can be drastically reduced.

4.7 Receiver Fabrication and Testing

The monolithic GaAs integrated circuit used as part of the receiver for this program was fabricated by the GaAs Integrated Circuits Section. The schematic design shown in Fig. 4.25 is realized by the direct implantation of Si for the FETs, diodes, and contact areas and the subsequent planar processing of these structures. The general processing scheme is shown in Fig. 4.26.

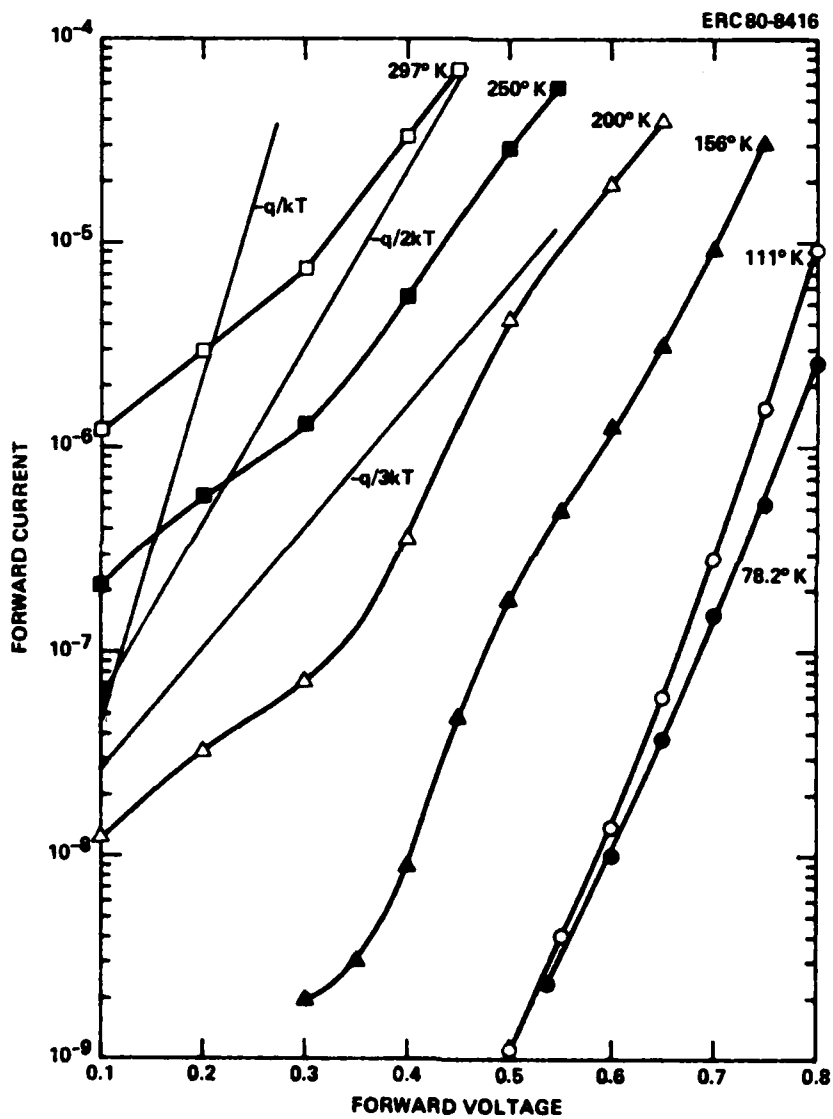


Fig. 4.23 The forward I-V characteristics of a GaAlAsSb APD at various temperatures.

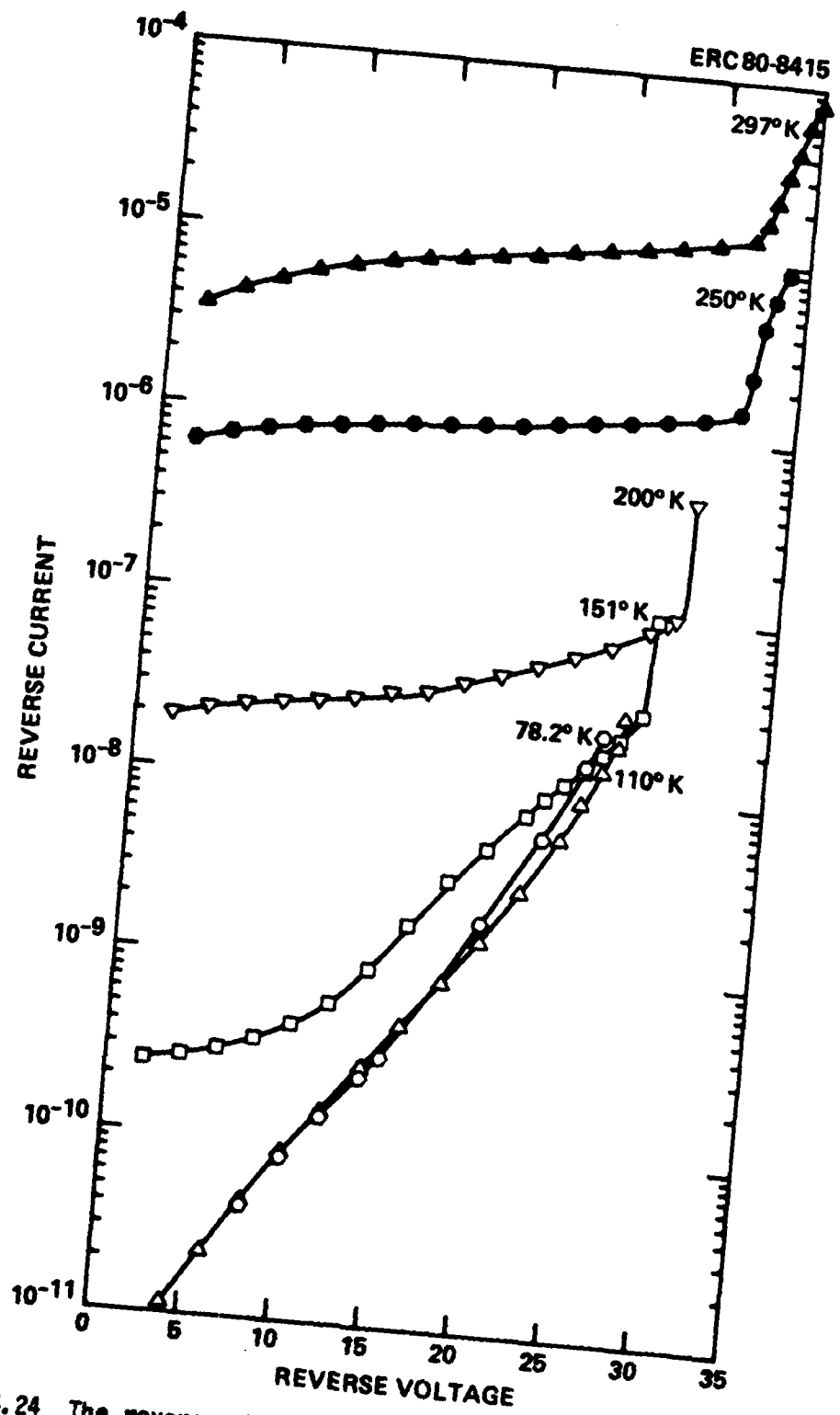


Fig. 4.24 The reverse characteristics of a GaAlAs Sb APD at various temperatures.

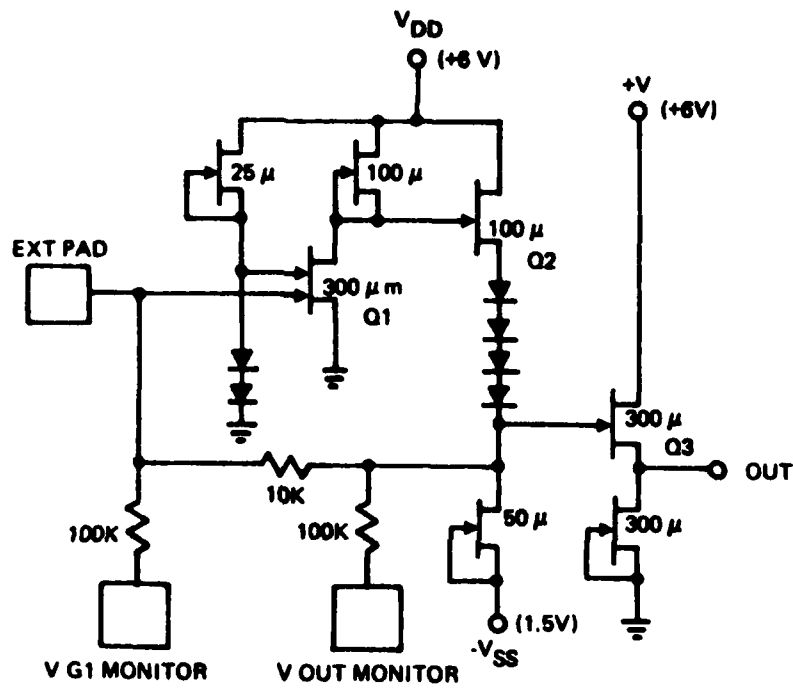


Fig. 4.25 Schematic diagram of photodiode preamplifier.

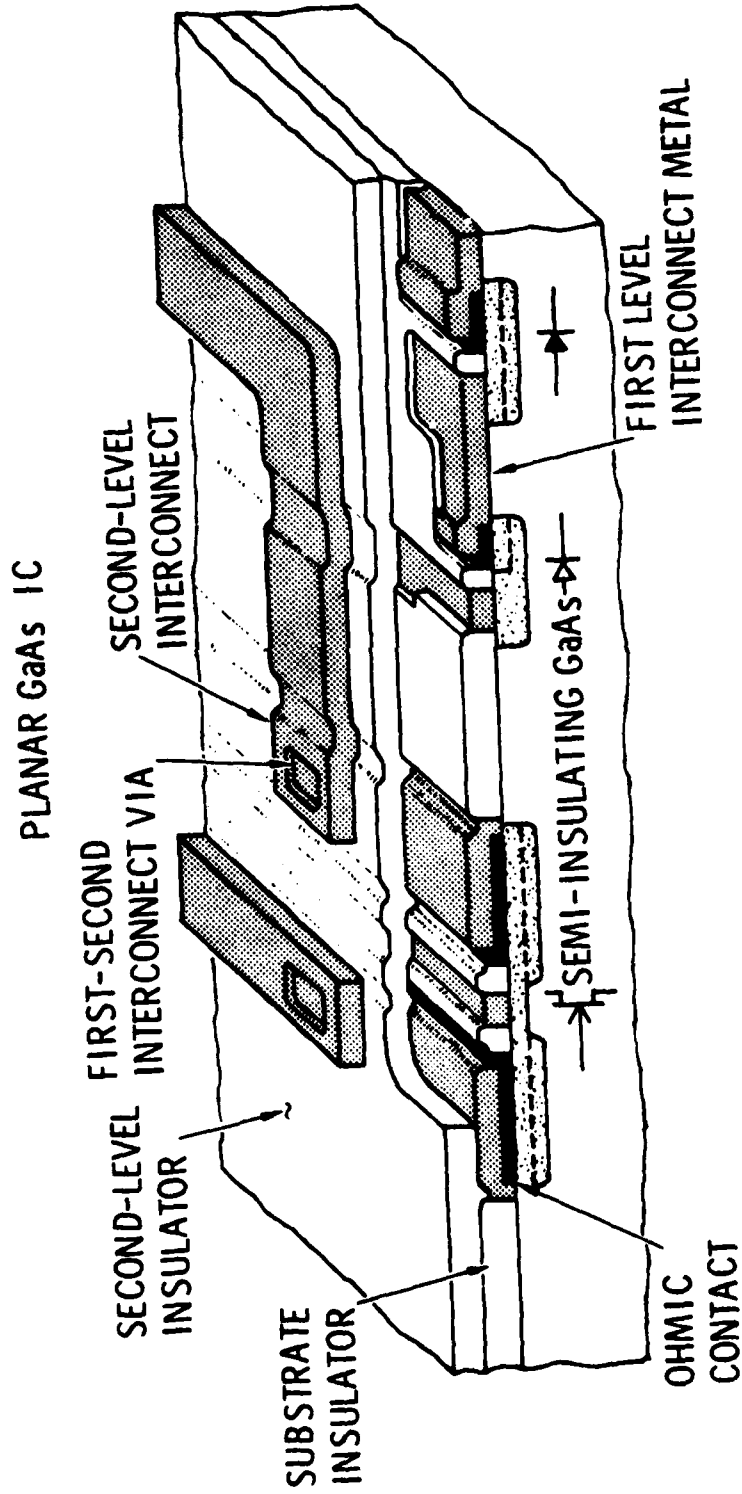


Fig. 4.26 Cut-a-way view showing two planar diodes and a planar FET and their interconnections.

This cross section photo shows that multiple implants are used for the FETs to define the contacts and channels and for the diodes to define the active and contact regions. A special metallization/isolation scheme is used to ensure planarity from one metallization level to another. This technique has been utilized to fabricate complex GaAs ICs with as many as 1,000 gates. The receiver is one of several test circuits fabricated on a mask set for process development. Figure 4.27 shows a photograph of a completed GaAs monolithic receiver. The batch fabrication of receivers has clear advantages over the hybrid fabrication technique. Some of these advantages are yield, uniformity, size and in production cost.

Wafers such as the one shown above were DC tested in wafer form to determine which of the amplifier circuits were operational. Circuits with higher feedback resistance were chosen for use. For example, the circuit tested below has a feedback resistance of 21.6 K Ω . This provides excellent transimpedance but limits the 3 dB cutoff frequency by $f_{3dB} = \frac{1}{2\pi RC}$, where C is the input capacitance. For this program, a bandwidth of 100 MHz is possible with this level of transimpedance.

Once the circuits to be tested were selected, the wafer was diced, and individual die were wire bonded in flat pack packages. These in turn were placed in special high frequency test blocks that serve as the interface to power supplies. The APD to be used is accommodated in a separate high speed package.

MRDC81-11548

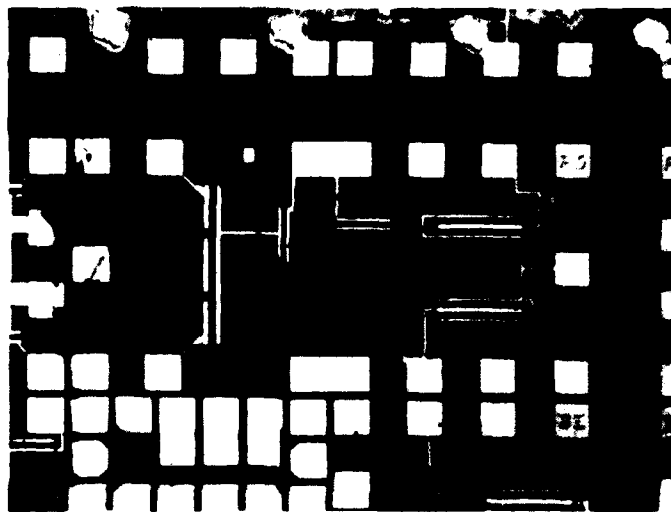


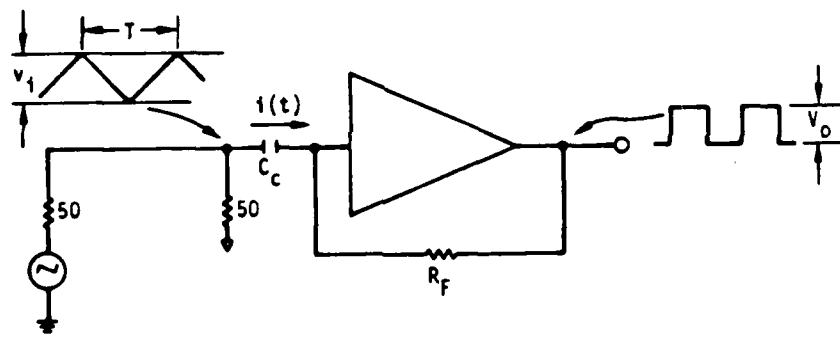
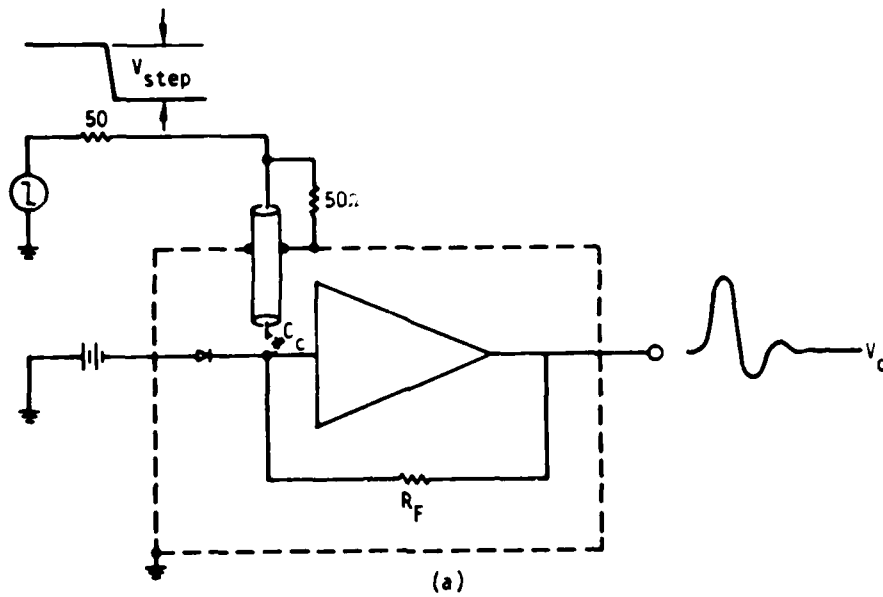
Fig. 4.27 Integrated optical receiver encircled by box.

An important parameter to be measured on a receiver is the open-loop gain-phase vs frequency. Unfortunately, this can only be measured by breaking the feedback loop. This is not practical in an integrated receiver, so all of the receiver testing was done in a closed loop configuration. The closed-loop frequency response of the receiver could be measured directly if a 100 MHz sine-wave modulated 1.3 μm light source was available. Since such a light source is not available at our laboratory, we have devised another technique for this measurement.

A special probe was fabricated in which a shielded cable was supported with its central conductor about 0.1 in. from the input point of the amplifier. Thus a small capacitance (C_c) was formed. The value of this capacitor was determined by injecting a triangular waveform and observing the output square wave. The value of C_c is then obtained as indicated in Fig. 4.28. This value was 10^{-14} F for the measurements described below.

The low frequency value of the effective feedback resistance or transimpedance is measured by inserting a known current from a signal generator through a 100K resistor into the preamplifier and measuring the output voltage of the first two stages at the V_{out} monitor with a high impedance scope. Figure 4.29 shows the waveforms that result from such a measurement. The transimpedance is then calculated from

$$R_o = \frac{V_{\text{out}}}{I_{\text{in}}} = \frac{V_{\text{out}}}{V_{\text{in}}} \cdot 100 \text{ k}\Omega = 21.6 \text{ k}\Omega$$



$$v_i = \frac{dv_i}{dt} \times t = \frac{dv_i}{dt} (T/2) \Rightarrow \frac{dv_i}{dt} = \frac{2v_i}{T}$$

$$v_o = R_o i(t) ; i(t) = C_c \frac{dv_i}{dt} \Rightarrow v_o = R_o C_c \frac{dv_i}{dt}$$

$$C_c = \frac{v_o}{R_o \left(\frac{dv_i}{dt} \right)} = \frac{v_o T}{2 R_o v_i}$$

(b)

Fig. 4.28 Schematic diagram of (a) probe set-up and (b) measurement technique for obtaining C_c .

MRDC81-12979

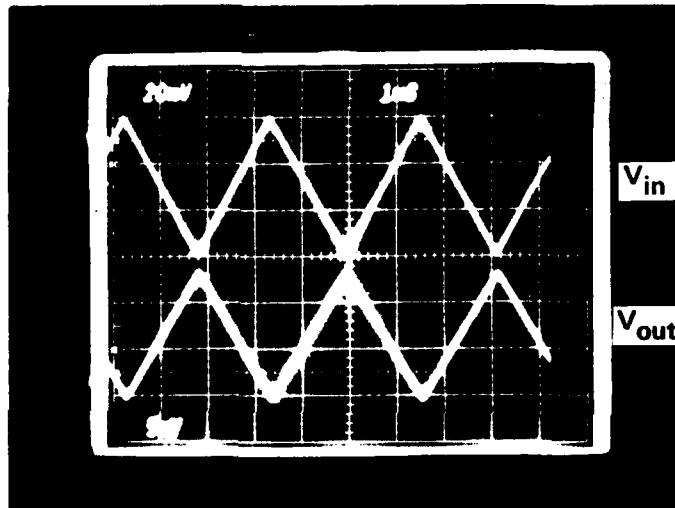


Fig. 4.29 Input and output voltages for first stage of pre-amplifier when a $100\text{ K}\Omega$ input resistor is used.

The gain of A_2 is determined from the ratio of the output of $A_1 \times A_0$ to the output of the preamp. A_2 was found to be $A_2 = 0.91$.

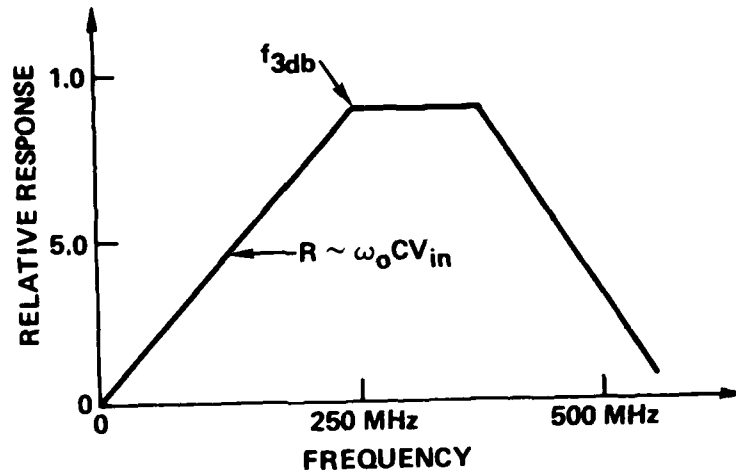
The frequency response of the receiver was measured by inserting a sinusoidal signal through the coupling capacitor from a swept frequency tracking generator. The output of the amplifier is coupled directly into the spectrum analyzer. Because the signal is capacitively coupled, the low frequency end of the frequency response approaches zero.

$$i_{in} = C_c \frac{dV_{in}}{dt} = C_c \frac{d}{dt} (V_{in}^0 \sin \omega t) = C_c \omega V_{in}^0 \cos \omega t .$$

To obtain the true frequency response of the preamp, it is necessary to divide the output by ω . Figure 4.30 shows the schematic representation of the capacitively coupled preamp (with 3 dB point indicated) as well as the actual frequency response of the capacitively coupled preamplifier from 0 to 200 MHz. The 50 MHz frequency transimpedance was found to correspond well with the value measured at ~ 1 KHz, i.e., 21.6 K Ω . The region from 0-50 MHz deviates from the expected variation in the schematic diagram. This is seen in all devices tested to date. Its cause is unknown. The 3 dB bandwidth is seen to be ~ 250 MHz. Of course, the usable bandwidth is considerably greater owing to the large transimpedance employed.

The apparent frequency response was found to be bias level dependent. Figure 4.31 shows the capacitatively coupled frequency response of this preamplifier at different bias and signal level conditions. The 3 dB

MRDC81-12878



(a)

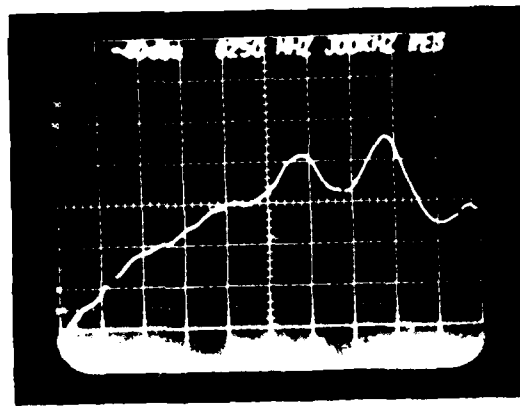


Fig. 4.30 (a) Schematic representation of relative preamp response vs frequency when capacitively coupled (b) Actual response of GaAs IC preamplifier.

MRDC81-12978

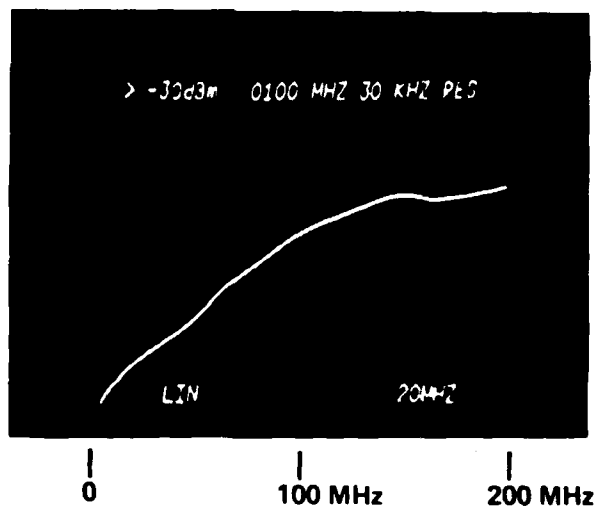
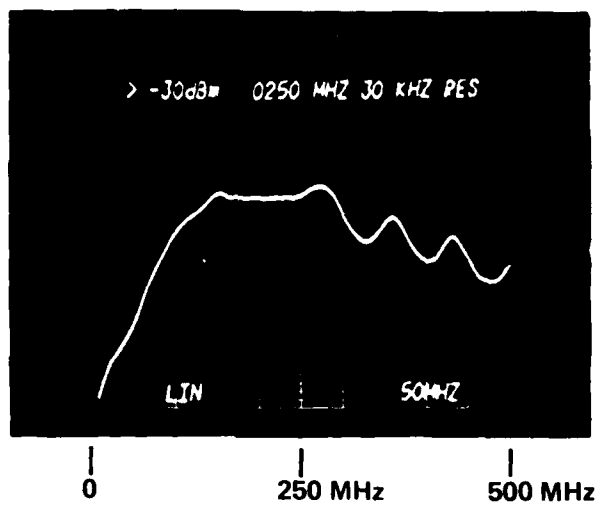


Fig. 4.31 Frequency response of capacitively coupled GaAs preamp under different bias condition than Fig. 4.30.

bandwidth here is shown to be 150 MHz. A possible cause for this is a signal and bias level dependence of the feed back resistor.

The most important noise measurement is the output spectrum since this allows us to make a detailed comparison with the spectrum predicted by the receiver model. The most convenient way to make this measurement has been to use a Tektronix 7L13 spectrum analyzer. This instrument has a calibrated vertical scale in both log and linear modes. In addition, the noise-bandwidth of the several resolution-bandwidth settings of the instrument has been calibrated. Thus the noise spectral density at any frequency is simply the actual measured noise amplitude divided by the square root of the noise-bandwidth of the resolution setting.

Another important measurement possible with the 7L13 is the direct measurement of noise equivalent current (NEI) from which noise equivalent power (NEP) can be computed. By definition, noise equivalent power is that power at which the signal is just equal to the noise. In general: $V_{sig} + noise = (V_{sig}^2 + V_{noise}^2)^{1/2}$; if $V_{sig} = V_{noise}$, then $V_{sig} + noise = \sqrt{2} V_{noise}$ and $20 \log V_{sig} + noise = 20 \log V_{noise} + 20 \log \sqrt{2} V_{s+n}(dB) = V_n(dB) + 3 \text{ dB}$. This can be performed at each frequency and the noise spectral density determined. The noise equivalent power is determined from the following

$$NEP = \frac{V_n h\nu}{q\eta R_o \sqrt{\Delta F}}$$

Figure 4.32 shows a plot of the NEP at various frequencies. At 100 MHz the
NEP = 1.45×10^{-13} W/Hz.

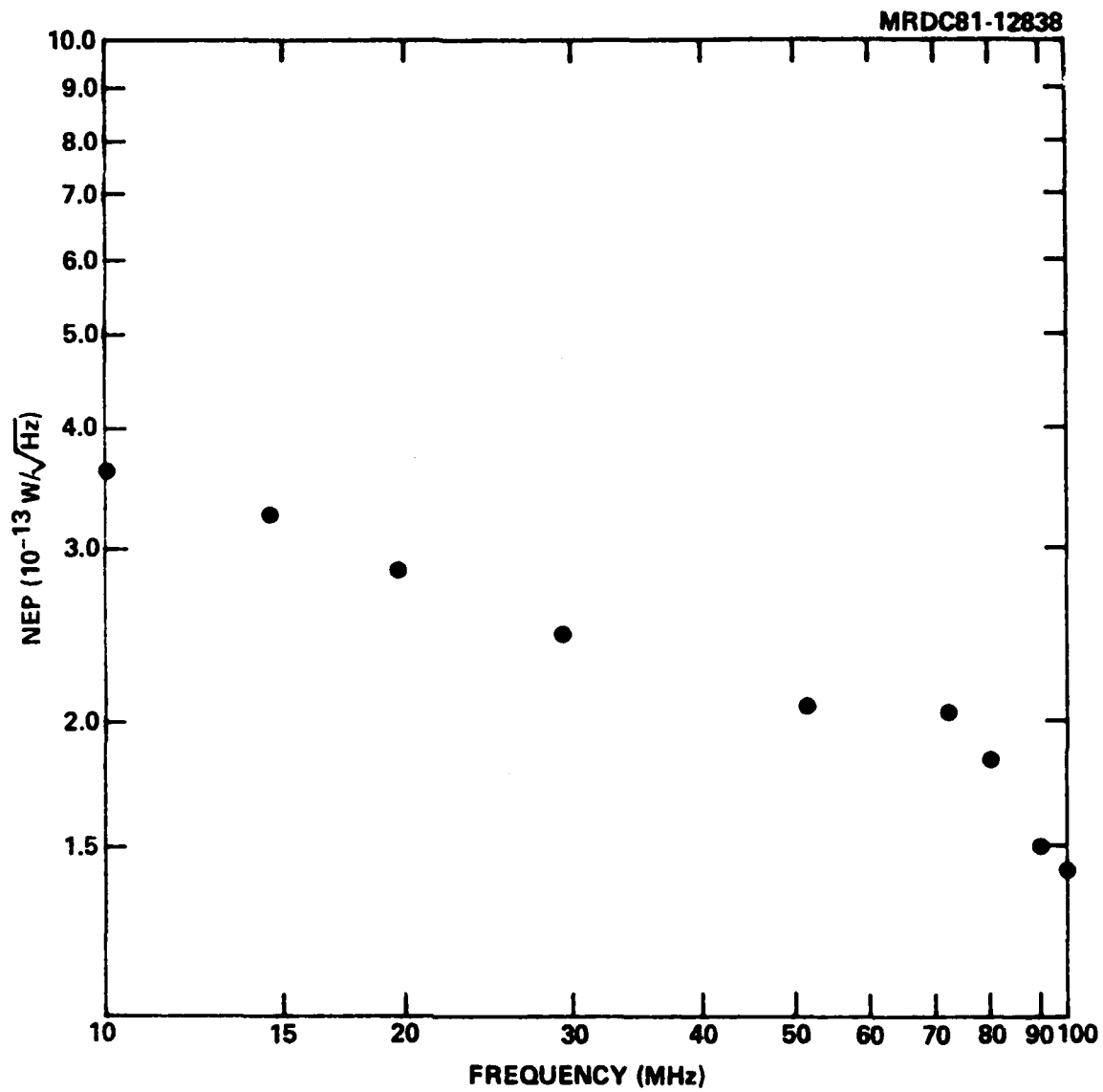


Fig. 4.32 Plot of NEP vs frequency.

5.0 CONCLUSIONS AND RECOMMENDATIONS

The results described in this report demonstrate that GaAlAsSb is a most attractive material for APD's at 1.3 μm . The high gains quantum efficiencies and speeds exhibited in a variety of device structures demonstrate its potential. The major problem remaining is related to materials growth uniformity and device surface leakage. The solution to these problems should be sought with intensive study. This system would then be most attractive for fiber optic receiver at 1.3 and 1.55 μm .

The GaAs monolithic preamplifier described in this report is capable of operating at frequencies in excess of 1 GHz with appropriate transimpedance. This is an ideal front end for a fiber optic communication receiver output or for an APD array. Further efforts to develop this receiver in a hybrid integrated format with APD's or pin devices should be undertaken.

Reference List:

1. H.D. Law, J.S. Harris, K.C. Wong, and L.R. Tomasetta; "GaAlAsSb/GaSb Alloys: Material Preparation and Applications to Optoelectronic Devices"; Inst. Phys. Conf. Ser. No. 45, Bristol, England: Inst. Phys. 1979, pp. 420-428.
2. G. Motosugi and T. Kagawa; "Liquid Phase Epitaxial Growth and Characterization of AlGaAsSb Lattice-Matched to GaSb Substrates"; J. Crystal Growth, Vol. 49, pp. 102-108, 1980.
3. M. Feng, M.M. Tashima, L.W. Cook, R.A. Milano, and G.E. Stillman; "The Influence of Growth Solution Dopants on Distribution Coefficients in the LPE Growth of InGaAsP"; Appl. Phys. Letter, Vol. 34, pp. 91-93, 1979.
4. S.J. Anderson, F.W. Scholl and J.S. Harris; "AlGaSb Alloys for 1.0-1.8 μ m Heterojunction Devices"; Inst. of Phys. Conf. Ser. #33b, Bristol, England; Inst. Phys. 1977, pp. 346-355.
5. H.D. Law, K. Nakano and L.R. Tomasetta; "III-V Alloy Heterostructure High Speed Avalanche Photodiodes"; IEEE, J. Quantum Electronics, Vol. QE-15, pp-549-558, 1979.
6. H. D. Law, Unpublished Data

MEMORANDUM

SUBJECT: [Illegible]

[Illegible text block]

**DAT
FILM**